THESIS FOR THE DEGREE OF DOCTOR OF PHILOSOPHY

Electrical Transport Properties of Nanostructured $SrTiO_3/LaAlO_3$ Interface

PIER PAOLO AURINO

Department of Microtechnology and Nanoscience
CHALMERS UNIVERSITY OF TECHNOLOGY
Göteborg, Sweden 2016

Electrical Transport Properties of Nanostructured $SrTiO_3/LaAlO_3$ Interface
PIER PAOLO AURINO

© PIER PAOLO AURINO, 2016

ISBN: 978-91-7597-454-5
Series number: 4135
Doktorsavhandlingar vid Chalmers Tekniska Högskola.
Ny serie (ISSN 0346-718X)

Chalmers University of Technology
Microtechnology and Nanoscience (MC2)
Quantum Device Physics Laboratory
SE-412 96 Göteborg, Sweden
Phone: +46 (0)31-772 1000

ISSN 1652-0769
Technical report MC2 – 346

Chalmers Reproservice
Göteborg, Sweden 2016

Electrical Transport Properties of Nanostructured $SrTiO_3/LaAlO_3$ Interface

PIER PAOLO AURINO
Department of Microtechnology and Nanoscience (MC2)
Chalmers University of Technology
Göteborg, Sweden 2016

Abstract

In 2004 Ohtomo and Hwang reported on the formation of a high mobility 2-dimensional electron gas (2DEG) at the interface between two wide band-gap insulators $LaAlO_3$ (LAO) and $SrTiO_3$ (STO). At least 4 unit cells (u.c.) of LAO need to be epitaxially deposited on top of a TiO_2-terminated STO substrate for the 2DEG to form. This 2DEG shows unique properties, such as two-dimensional superconductivity, giant electric field effect, and the possible co-existence of ferromagnetic and superconducting phases. Many studies reported evidences of the non-homogeneous nature of the interfacial 2DEG, both regarding in-plane carrier distribution and magnetic properties. As such, the LAO/STO 2DEG represents a very complex electronic system, with many degrees of freedom.

The main goal of this PhD work is to investigate the electrical transport of nanoscale structures formed in the LAO/STO interface and to shed more light on the complex nature of this system and its phase diagram. To realize this goal, the development of a robust and reliable technique to pattern the 2DEG at the LAO/STO interface is a prerequisite, this constitute the first part of the project. We have observed a metal-insulator transition (MIT) at the LAO/STO interface using irradiation by low energy Ar ions. Such irradiation-induced MIT was used in combination with optical and e-beam lithography to pattern structures down to 50 *nm*. A detailed study of the effect of low-energy Ar^+ irradiation on the LAO/STO interface is presented, as function of irradiation energy, irradiation time, and film thickness. We report the full reversibility of the MIT by high temperature annealing. With the help of x-ray photoelectron spectroscopy (XPS) and scanning transmission electron microscope (STEM) we show that the origin of the MIT can be explained by Ar implantation.

In the second part of the thesis, electrical measurements on nanostructures in the LAO/STO interface are presented. We show a significant increase of sheet resistance with decreasing structure size below 1 μm. We relate this observation to the innate non-homogeneity in the 2DEG at LAO/STO interface. A recent work demonstrated that is possible to improve the electrical conductivity of the interface by adding a $SrCuO_2$ (SCO) layer on top of the LAO/STO. We investigated the effect of adding a SCO capping layer on the LAO/STO before the nanostructures are patterned. We observed that the conductivity of macroscopic structures is improved by the capping layer in a similar way to the original report. The behavior of nanoscale structures also changes, and electrical properties of nanostructures are comparable to micrometer size structures. This allowed us to investigate electrical transport properties in SCO capped nanostructures at low temperature and under magnetic field. We report for the first time a superconductive transition in the SCO capped nanostructures. Furthermore, it is found that SCO capped nanorings show a SQUID-like behavior. We discuss the possible relations between the observed results and the non-homogeneous nature of the 2DEG.

Keywords: Complex Oxides, Interfaces, Thin Films, LAO/STO, 2DEG, Nano-Patterning, Ar Ion Implantation, superconductivity, Nanodevices.

This thesis is based partly on the following scientific papers:

I. ***"Nano-patterning of the electron gas at the $LaAlO_3/SrTiO_3$ interface using low-energy ion beam irradiation"*** Aurino, P.P.; Kalabukhov, A.; Tuzla, N.; Olsson, E.; Claeson, T.; Winkler, D.; *App. Phys. Lett.*, **102**, 201610, (2013).

II. ***"Reversible metal-insulator transition of Ar-irradiated $LaAlO_3/SrTiO_3$ interfaces"*** Aurino, P.P.; Kalabukhov, A.S.; Tuzla, N.; Olsson, E.; Klein, A.; Erhart, P.; Boikov, Y.A.; Serenkov, I. T.; Sakharov, V.I.; Claeson, T.; Winkler D.; *Phys. Rev. B*, **92**, 155130, (2015).

III. ***"Retention of electronic conductivity in LaAlO3/SrTiO3 nanostructures using $SrCuO_2$ capping layer"*** Aurino, P.P.; Kalabukhov, A.; Borgani, R.; Haviland, D.; Bauch, T.; Lombardi, F.; Claeson, T.; Winkler, D.; *Phys. Rev. Applied,* **6,** 024011, (2016).

IV. ***"Unconventional superconducting correlations at the interface between $LaAlO_3$ and $SrTiO_3$***" Aurino, P.P.; Kalabukhov, A.; Galletti, L.; Bauch, T.; Lombardi, F.; Claeson, T.; Winkler, D.; manuscript.

V. ***"Non-destructive cleaning of the $LaAlO_3/SrTiO_3$ surface with ultraviolet light and ozone."*** Andersson, E.; Aurino, P.P.; Winkler, D.; Kalabukhov, A.; *J. of Vac. Sci. and Technol. B* **34**, 041201, (2016).

VI. ***"Hardening of the soft phonon in bulk $SrTiO_3$ interfaced with $LaAlO_3$ and SrRuO"*** Nucara, A.; Ortolani, M.; Baldassarre, L.; Mohamed,W. S.; Schade, U.; Aurino, P. P.;Kalaboukhov, A. S.; Winkler, D.; Khare, A.; Miletto Granozio, F.; Calvani, P.; *Phys. Rev. B,* **93**, 224103, (2016).

Individual contribution to every publication:

I. AK and PPA developed the idea, did the sample fabrication and performed the electrical measurements. NT and EO did the STEM imaging. PPA did the data analysis with inputs from AK, wrote the paper with inputs from all the co-authors and completed the submission process.

II. AK and PPA developed the idea. PPA did the sample fabrication, performed the electrical measurements and AFM imaging and relative data analysis. NT and EO did the STEM imaging and relative data analysis. AKl did the XPS. PE did the theory (DFT). YuB, IS and VS did the MEIS analysis. PPA wrote the paper with inputs from all the co-authors and completed the submission process.

III. AK and PPA developed the idea. PPA did the sample fabrication and performed the electrical measurements and AFM imaging. RB, DH, AK and PPA did the Kelvin probe AFM. TB and PPA did the low temperature measurements. PPA did the data analysis, wrote the paper with inputs from all the co-authors and PPA will complete the submission process.

IV. AK and PPA developed the idea. PPA did the sample fabrication. LG and PPA did the low temperature measurements. PPA did the data analysis, is writing the paper with inputs from all the co-authors and, will complete the submission process.

V. AK, EA and PPA developed the idea. EA and PPA did the sample fabrication. EA did the data analysis. EA wrote the paper with inputs from all the co-authors and completed the submission process.

VI. AK and PPA collaborated to this paper by fabricating the samples, and participating to the discussion of the experiment. Paper was written by PC and his collaborators at University of Rome.

List of abbreviations and symbols

AFM	atomic force microscopy
ALD	atomic layer deposition
CVD	chemical vapor deposition
EELS	electron energy loss spectroscopy
EDS	energy dispersive X-ray spectroscopy
e^-	electron charge
ImEFM	Intermodulation electrostatic force microscopy
LAO	$LaAlO_3$
MIT	metal-insulator transition
MBE	molecular-beam epitaxy
PLD	pulsed laser deposition
PSC	Phase slip centers
q2DEG	quasi two-dimensional electron gas
RHEED	reflection high-energy electron diffraction
SCO	$SrCuO_2$
SCD	Switching current distribution
SRIM	stopping and range of ions in matter
STEM	scanning transmission electron microscope
STO	$SrTiO_3$
TEM	transmission electron microscope
THz	terahertz
UV	ultra-violet light
u.c.	unit cells
XPS	x-ray photoelectron spectroscopy
β_L	screening parameter
λ_L	London penetration depth
ξ	Coherence length
Ω/□	Ohm per square unit

Table of Contents

1 Introduction

Over recent years, complex oxides attracted more and more researchers, both from the condensed matter physics and from the materials science communities. Complex oxides play a key role to realize new functionalities and to achieve further miniaturization, improving future devices in emerging markets. Complex oxides exhibit a plethora of interesting macroscopic physical properties (such as conductivity, dielectricity, transparency, optical non linearity, ferroelectricity, high T_c-superconductivity, colossal magneto-resistivity, piezoelectricity, etc.) and wide research efforts are dedicated on growing and combining oxide films and heterostructures. The complexity of the physics involved triggered intense studies aimed at understanding the fundamental nature of existing systems; at the same time, several attempts have been made to design and control new materials for practical applications. Moreover, techniques such as pulsed-laser deposition (PLD) and molecular-beam epitaxy (MBE) have been constantly improving, providing powerful tools to create layered structures of these complex oxides.

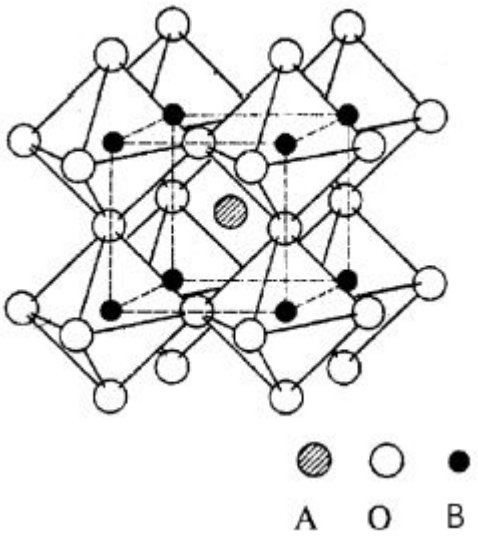

Figure 1.1 Schematic illustration of an ideal Perovskite crystal lattice structure. The real crystals can present rotations, tipping, and elongations of the oxygen octhaedra.

Several metal oxides crystallize in a common way creating a class of crystalline structures called perovskites. Usually those materials follow the structure ABO_3 [1], where the smaller B atoms, usually transition metals, form cubic cells centered around bigger A atoms, usually alkali metals; Oxygen atoms, O form octahedral structures surrounding the B atoms (see Fig. 1.1) [2].

The present work deals with a special system formed by two renowned perovskites oxides: the strontium titanate ($SrTiO_3$) and the lanthanum aluminate ($LaAlO_3$), both wide band-gap insulators. The interface between these two oxides shows interesting and unique properties.

1.1 Thin films of complex oxides

The properties of complex oxides become even more interesting when they are engineered in order to exploit the nanoscale and interface effects (super-lattices, nanowires, etc.).

The first challenge in this direction is the growth of such materials that can be very delicate due to precise demands with respect to chemical composition, high temperature needed for epitaxy, and crystalline quality. The most common techniques used to deposit complex oxides thin layers are pulsed laser deposition (PLD) [3], molecular beam epitaxy (MBE) [4], chemical vapor deposition (CVD) [5], magnetron sputtering [6] and atomic layer deposition (ALD). Usually the CVD requires sophisticated chemical reactors. Sputtering provides high films quality, but it is restricted to a narrow range of parameters, such as pressure. MBE provides the highest quality films but has very slow growth rates, it is expensive and not flexible. ALD can be very slow too and it is generally used in industrial production of very thin layers. PLD is a very flexible technique and is therefore mainly used for research purposes, where one wants to easily vary different deposition parameters. For the deposition required in our experiments we used the PLD technique, as it will be described in details in Chapter 3.

It is important to mention that complex oxide thin films are not yet very popular in industry for common use; the main reason is that the properties of these materials change over several orders of magnitude with only slight shifts in material composition, crystallinity, or morphology. This extreme variability in properties is then both a strength and a weakness, and highly precise deposition processes are required to achieve reproducible results. Achieving this kind of knowledge and control over the system of complex oxides is therefore the key to open a new world of industrial applications.

1.2 Motivations of the thesis

The present work is focused on the notable system formed by $LaAlO_3$ (LAO) and $SrTiO_3$ (STO). Both LAO and STO are non-magnetic wide band-gap insulators, nevertheless the LAO/STO interface exhibits properties such as high electrical conductivity [7], superconductivity [8], ferromagnetism [9], large in-plane magnetoresistance [10] and giant persistent photoconductivity [11].

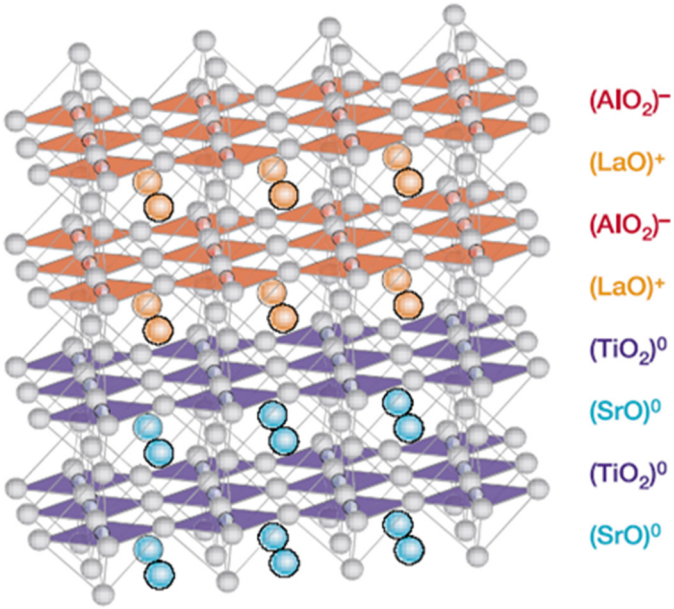

Figure 1.2 Schematization of the LAO/STO conductive interface. (from *A. Ohtomo, H. Hwuang, Nature 427, (2004)*).

The studies of the LAO/STO interface indicate that the conductivity is two-dimensional and thus it is commonly referred to as a two-dimensional electron gas (2DEG). The possibility to pattern the 2DEG on nanoscale would open the opportunity to design structures on the same scale as characteristic physical lengths of the system, such as the Fermi wavelength and electron mean free path; in this case, quantum effects may occur. Controlled engineering of the LAO/STO interface is the key to open this system to the electronic industry [12] [13], and scaling down to nanometers will enable to design devices based on quantum physics (e.g. field effect devices, nanoscale photodetector etc.). Understanding the phases of strongly correlated electron systems such as the 2DEG formed at the LAO/STO interface is of fundamental interest. One of the most interesting questions is if the same electrons in the 2DEG are participating in both magnetic and superconducting ordering. If this is the case, the superconductivity may have an exotic chiral p-wave character. Such an unconventional superconducting state has been a long-sought phenomenon in condensed matter physics. A two-dimensional p-wave superconductor can host Majorana bound states that may be attractive in topological quantum computation. Superconducting and magnetically ordered electrons may also occupy separate electronic bands. In this case, superconductivity in the LAO/STO interface should have a traditional s-wave character mediated by electron-phonon coupling. However, it might still be possible to induce unconventional pairing by external electric field when spin-orbit coupling overcomes the superconducting gap. The system is further complicated by an non-homogeneous nature of metallic and superconducting states. There is evidence of percolative superconductivity and possible pre-formation of Cooper pairs above the “bulk” critical temperature.

As such, the LAO/STO interface becomes a unique playground to study interconnections and competitions between the different ordering phenomena in an unconventional strongly correlated two-dimensional electron gas.

The goal of this work was to design and investigate structures on the nanoscale in order to shed more light on the electronic properties of the LAO/STO system. Several studies report evidences of non-homogeneities in the 2DEG electrical conductivity. Our aim was to design structures with size approaching the dimension of these non-homogeneities, creating devices that exploit the innate quantum properties of the system.

To do so we first needed to achieve a reliable technique to pattern the 2DEG. While the main focus for researchers studying the LAO/STO interfacial system remains the understanding of the 2DEG formation, in the latest years a number of studies focused on the developing of patterning techniques. Many attempts have been done but most of the existing techniques present substantial drawbacks, as we will discuss more in detail in Chapter 2, mainly due to the use of highly invasive methods or results that are not stable over long periods of time. In the first part of this work we will present the study and application of a novel technique for patterning the 2DEG at the LAO/STO interface, which can produce robust and reliable structures down to the nanoscale. With our technique we were able to pattern nanostructures down to 50 *nm*. At these dimensions we could expect effects of the quantum properties of the LAO/STO system on our structures. The second goal was then to design the appropriate structures for such a purpose, to investigate their properties and to try to understand the physics observed. Our work gives new insights on the working mechanisms of the LAO/STO system, and at the same time opens interesting doors to novel applications (such as nanoscale sensors, non-volatile memories etc.).

1.3 Thesis structure

In the second chapter of this thesis we will describe in detail the LAO/STO system: under which conditions the 2DEG is formed, what are the main models describing the system, how to improve the electrical properties of the system using a $SrCuO_2$ capping layer, and what the existing patterning techniques are.

In the third chapter we will describe the experimental setup and procedures performed in order to obtain the LAO/STO interfaces we used in our experiments.

In the fourth chapter we will report the possibility to induce metal-insulator transition at the LAO/STO interface using low energy Ar^+ ion irradiation, and we will present a study of the effect of the irradiation on the LAO/STO interface. We will also show that is possible to restore the initial metallic state using a high temperature annealing process.

In the fifth chapter we will describe how the irradiation can be used in conjunction with optical or e-beam lithography to pattern structures in the 2DEG at the LAO/STO interface. Moreover we will have a brief overview of complementary experiments.

In the sixth chapter we will describe electrical properties observed in nanostructures. We will report the effects on LAO/STO nanostructures of adding an $SrCuO_2$ capping layer and we will present the observed squid-like behavior in nanorings.

In the last chapter we will present a critical discussion of our work and summarize the results of the thesis.

2 The LAO/STO system

In this chapter we will describe the physics of the LAO/STO interface. We will introduce the most important properties of this system and, at the same time, we will present an overview of the different models used to explain the formation of the electron gas at the interface. In the last part we will review the already existing techniques used to pattern the interface, pointing out their advantages and disadvantages.

2.1 LAO/STO interface

The formation of a high-mobility electron gas at the LAO/STO interface was reported for the first time by Ohtomo and Hwang in 2004 (see Fig. 2.1) [7]. They also found that the electron gas is only formed when the interface is *n*- type, *i.e.* when the LAO is

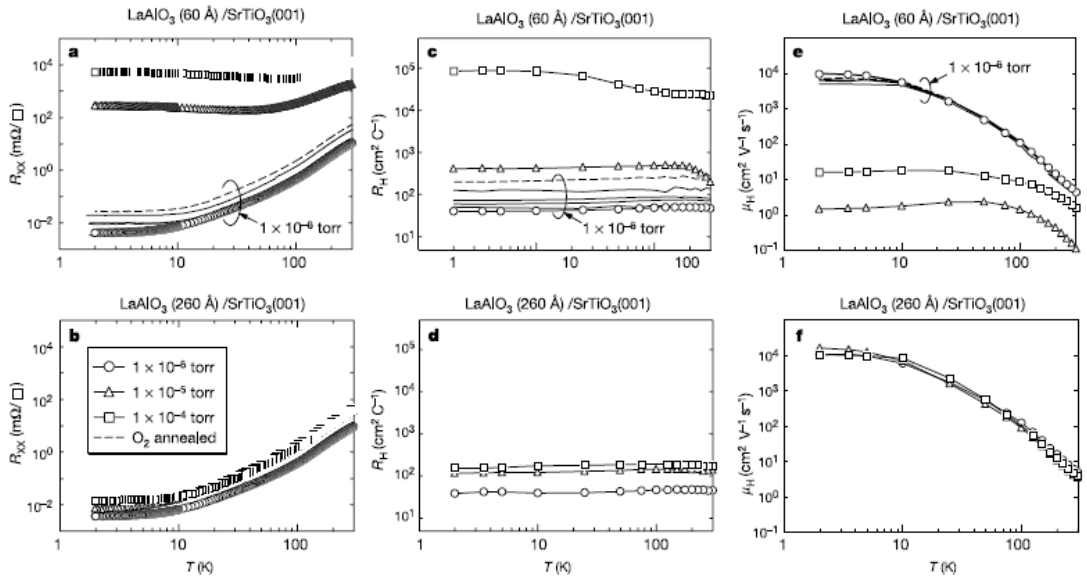

Figure 2.1 Electrical properties of the LAO/STO interface as a function of different oxygen pressures during growth of the LAO film, as first reported in *A. Ohtomo, H. Hwuang, Nature 427, (2004),423-426*. Data reported show the sheet resistance R_{XX}, the Hall coefficient R_H and the Hall mobility μ_H, for a 6 *nm* thick LAO film in a), c) and e) respectively, and fora a 26 *nm* thick LAO in b), d) and f). These measurements showed for the first time evidence of a conductive state at the LAO/STO interface.

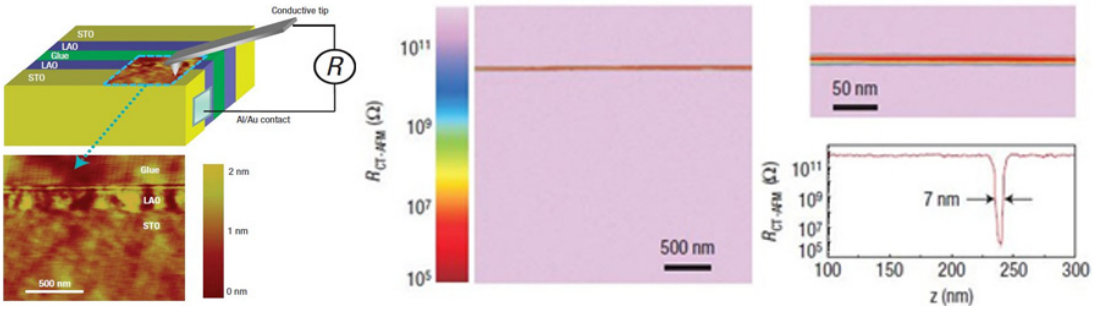

Figure 2.2 Experimental setup for conductive-tip atomic force microscope (AFM) measurements (left), and mapping of the spatial distribution of electrical conductivity at the LAO/STO interface. (from *M. Basletic et al., Nature Materials, 7, (2008), 621 - 625*). The measurement shows that the conductivity is confined in the first 7 *nm* inside the STO substrate.

epitaxially grown on an STO substrate with TiO_2 surface terminations; the *p*- type interface, formed when the STO surface is SrO terminated, is nevertheless insulating. The conductive state has been suggested and experimentally confirmed to be a two-dimensional electron gas (2DEG) [14] [15], localized in the first few unit cells (u.c.) inside the STO substrate if properly post-annealing in oxygen atmosphere (see Fig. 2.2). In the case the interface is formed at very low oxygen pressure, the conducting layer can extend at least a micron in the STO [16]. Annealing in high oxygen pressure of the sample after the deposition can also modify its electrical properties. The behavior of the system slightly deviates from the expected one for a perfect 2DEG where the electrons are free to move in two dimensions, but tightly confined in the third, for this reason it is often referred to as *quasi* two-dimensional electron gas (q2DEG).

The conductivity at the LAO/STO interface appears only when specific conditions are fulfilled, such as: the STO substrate is TiO_2 terminated [7] and the LAO is at least 4 u.c. thick [17]. It is widely reported that when the LAO film thickness is below 4 u.c., the interface is insulating (see Fig. 2.3). Whereas a sharp transition from insulating to metallic state happens precisely at 4 u.c., both electrical conductivity and carrier concentration are nearly constant as the LAO film thickness is further increased. Other experiments reported formation of the interfacial q2DEG under different conditions, such as when 1 u.c. of LAO is grown epitaxially on an STO substrate, and then an STO film is grown on top of the LAO [18]; in this case it is the STO film that shows a critical thickness of around 4 u.c. required for the formation of the q2DEG. The formation of the q2DEG has been reported [19] also for different orientation of the LAO crystal lattice, nominally (110) and (111) showing a critical LAO film thickness of 7 and 9 u.c., respectively.

Another fundamental parameter for the formation of the q2DEG is the LAO stoichiometry. It has been shown [20] that the q2DEG is formed only if the La/Al ratio is below 1, nominally ~0.9.

Additional studies of the LAO/STO interface showed very rich physics, including two-dimensional superconductivity [8], magnetic phases [21], giant electric field effect [16], and ferromagnetic ordering [9] [22]. The mechanism of the

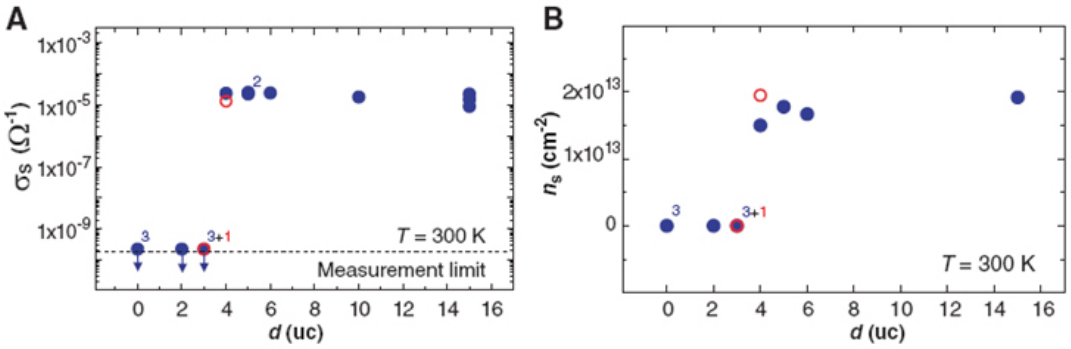

Figure 2.3 Dependence of A) sheet conductance and B) sheet carrier density as function of the number of LAO u.c. deposited. (from *S. Thiel et al., Science vol. 313(2006)*). These data show the presence of a 4 u.c. thickness threshold.

formation of the q2DEG at the LAO/STO interface has been widely debated. Different models have been proposed during the years to explain these phenomena; however, none of them is yet fully accepted by the research community or can explain all the experimental evidences that sometime even show controversial results.

One of the most common explanations is known as the polar catastrophe model; it is based on the fact that the sequence of layer in the STO substrate is terminated by a top TiO_2 with neutral polarity, while the LAO film starting with a LaO layer has a positive polarity, thus creating a polar discontinuity at the interface [23]. The discontinuity results in the formation of a growing electrostatic potential that increases with the increasing of the LAO layer thickness, diverging eventually to infinity. The model claims that at some point the potential will grow enough to move electrons from the surface of the LAO layer back to the LAO/STO interface (the so called polar catastrophe [7]) leading to an electronic reconstruction at the interface (see Fig. 2.4). This model is in good agreement with the experimental observation of a threshold thickness of LAO film required for the formation of the q2DEG.

Another hypothesis is that the conductivity can be explained by the presence of free electrons coming from oxygen vacancies in the STO [24] [25] [26]; presence of such vacancies has been emphasized in many studies and it is known that oxygen vacancies can dope the STO substrate. It is established that oxygen vacancies in the STO substrate are produced during the growth of the LAO film and this can gives rise to the electrical conductivity. Addressing the origin of the q2DEG only to the

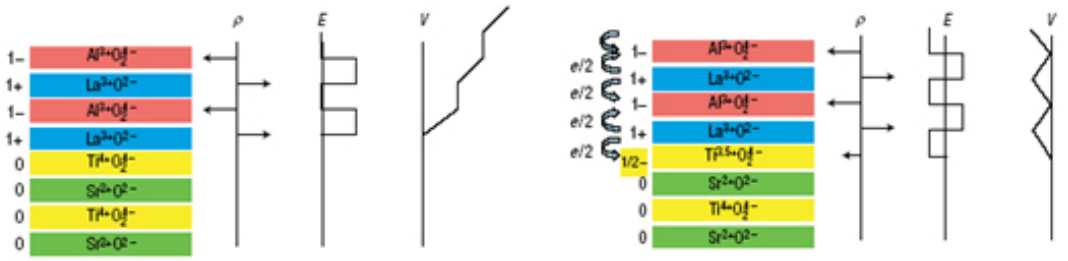

Figure 2.4 Schematic illustration of the formation of diverging potential and subsequent electronic reconstruction at the interface of LAO/STO as described within the polar catastrophe model. (from *N. Nakagawa et al., Nature Materials 5, 204 - 209 (2006)*).

presence of oxygen vacancies one would expect that samples grown at low oxygen pressure have a high charge density n. This is indeed experimentally found, with very high densities in the order of $n{\sim}10^{17}cm^{-2}$at low oxygen pressure. However, samples grown at high oxygen pressure still show charge density of $n{\sim}10^{13}cm^{-2}$and this state is resistant to high oxygen pressure post-annealing.

The intermixing models suggest that the La^{3+} from $LaAlO_3$ diffuses into the $SrTiO_3$ substrate occupying Sr^{2+} sites and donating electrons [27] [28]. Several studies have shown that intermixing takes place at the interface, however it is doubtful if the extent of the intermixing is enough to be considered the main origin of free carriers.

Recently a new polarity-induced defect mechanism has been proposed using first principles defects calculations [29]. This model claims that the polar discontinuity across the interface thermodynamically triggers the spontaneous formation of defects; the Ti-Al defects, created below 4 u.c., compensate the polar discontinuity, while the surface donor defects (oxygen vacancies), created above 4 u.c. donate electrons to the interface. The q2DEG originates from the oxygen vacancies but the charge carrier density of the q2DEG is controlled by the interfacial deep acceptor defects, Al-on-Ti antisites.

Finding a definitive answer to the debate about the origin of the q2DEG formation at the LAO/STO interface is outside the scope of this work. Nevertheless our work will possibly put in place some of the pieces of this puzzle, stimulating further discussion and participating in the solution of the problem.

2.2 $SrCuO_2$ capping layer

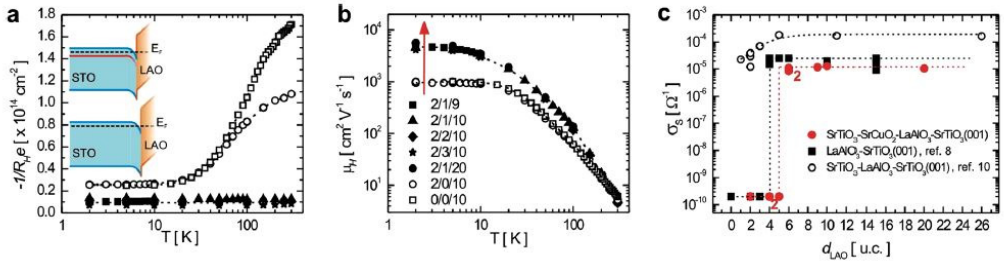

Figure 2.5 Effects of a $SrCuO_2$ capping layer on conductivity and mobility temperature dependencies of the LAO/STO interface. Experimental data are reported for several combinations of STO/SCO/LAO layer thicknesses where the numbers express the thickness in u.c. (from *Huijben, M. et al., Adv. Funct. Mat., 2013, 5240-5248*)

It was shown recently [30] that adding a $SrCuO_2$ (SCO) capping layer on the top of the LAO, improves electrical properties of the q2DEG. The authors claim that the SCO capping layer is enhancing the oxygen exchange and so reducing the oxygen vacancies, resulting in a decreased scattering of the carriers at the interface. An additional STO layer can be deposited on the top of the SCO to protect it from chemical contaminations. The authors report results (see Fig. 2.5) for several

combinations of the thickness of the STO/SCO/LAO layers, showing that 1 u.c. of SCO is enough to increase electrical conductivity and mobility. It is important to notice that the samples presented in [30] are not post-annealed, and that the authors report an increase of the critical thickness to 6 u.c. of LAO in case of capped samples.

We take advantage of the SCO capping to enhance the properties of our samples; we will describe in Chapter 6 how the presence of the SCO capping layer not only affects the properties of the LAO/STO interfacial q2DEG on large scale but also changes electrical transport properties of nanostructures. We show that sheet resistance of the uncapped LAO/STO structures increases when dimensions decreases below 1 μm, and that this can be related to non-homogeneities in the q2DEG. We report that for SCO capped structures this size dependence of the sheet resistance disappears and the nanostructures retain their electrical properties with values almost identical to micrometer sized structures.

2.3 Non-homogenous nature of the q2DEG

Several independent works reported evidence of non-homogeneity of the q2DEG, both about the electrical transport distribution and the presence of ferromagnetic patches in a uniform paramagnetic background [31] [32] [9]. There is still no microscopic model that explains how ferromagnetic and superconducting ordering co-exists in the LAO/STO q2DEG. Monte Carlo simulations show that oxygen vacancy defects may form clusters and "ferromagnetic puddles" spatially separated from superconducting areas [33]. Recent studies have proposed a possible non-homogeneous superconducting state where superconducting islands with randomly distributed critical temperatures are embedded in a matrix of weakly localized electrons [34]. The presence of high- and low-mobility carriers in similar systems such as $LaTiO_3/SrTiO_3$ were revealed by magneto-transport experiments, and superconductivity seems to develop there as soon as high-mobility carriers appear [35] [36]. When temperature is lowered, the electrical resistance is reduced, and signatures of a superconducting fraction can be seen above the temperature at which the global zero resistance state is reached. The characteristic size of the non-homogeneities was estimated from scaling arguments to be around 100 *nm* [37] [38]. Such phase separation should have very strong influence on the electronic transport in nanoscale structures, and the effect of the non-homogeneous electrical transport will be most pronounced in structures having width comparable to the average size of the non-homogeneities.

In our experiments we designed structures with dimensions down to 100 *nm* in order to investigate the effect of those non-homogeneities on the electrical transport properties of the narrow structures. In the last part of this thesis we describe an innate SQUID-like behavior and other non-conventional features observed in SCO capped LAO/STO nanorings.

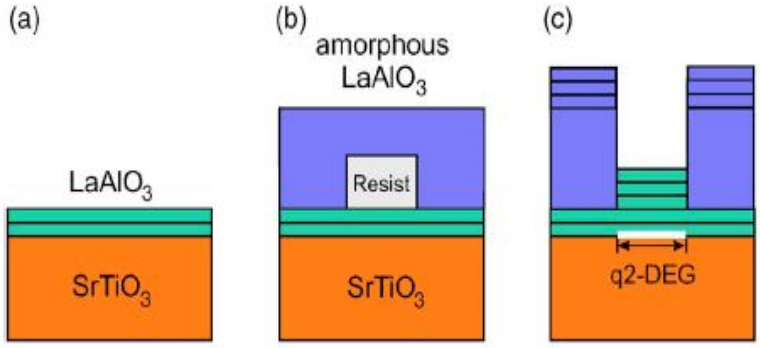

Figure 2.6 Schematization of the process of patterning using an amorphous $LaAlO_3$ layer as mask as proposed in *C. Schneider, et Al., Appl. Phys. Lett., 2006.*

2.4 Patterning of the LAO/STO interface

The plethora of properties exhibited at the LAO/STO interface, and the desire to design devices to utilize those functional properties, creates a great interest in the possibility of patterning the conductive q2DEG. A reliable technique to fabricate structures in the q2DEG on the nanoscale is fundamental both to understand the physics underlying the LAO/STO interface conductivity, and to open the door to possible applications on large scale.

A straightforward way to pattern the interface would be to physically remove the LAO film by chemical or dry etching [39], or using a lift-off process. Chemical etching of the LAO film is rather complicated as it is difficult to find durable materials that will resist aggressive acids required for the etching of the LAO film. Ion beam etching of the LAO/STO interface is not viable because an ion beam with the energy required to etch the LAO film may also produce oxygen vacancies in the STO substrate [40]. This would result in electrical doping of the STO substrate and therefore electrically shunt the q2DEG at the LAO/STO interface [41] [42]. Another

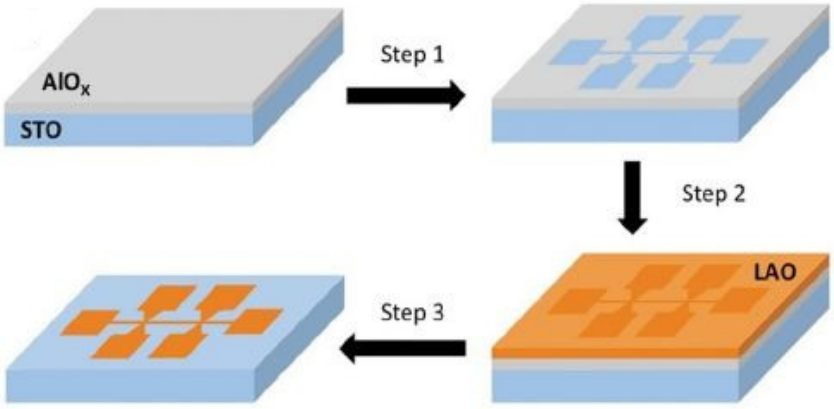

Figure 2.7 Schematic illustration of the lift-off patterning of the LAO/STO interface using amorphous AlOx film, as described in *N. Banerjee, et al., Appl. Phys. Lett., 2012, 041601.*

possible way to pattern the LAO film is by a lift-off process. In this process, the lift-off polymer mask is patterned prior the film deposition. After deposition, the mask is dissolved, leaving film only on uncovered areas. However, the very high temperature (800 ºC) and oxygen atmosphere pressure used during the deposition of the LAO film destroy polymer masks typically used in a standard lift-off process.

As an alternative solution, several hard lift-off masks have been suggested. For example, 2 u.c. of LAO were deposited epitaxially on an STO substrate forming an insulating layer (see Fig. 2.6). Then a polymer resist was patterned on the surface and an amorphous LAO film was deposited at room temperature as a protection layer on the top. The resist was lifted off, leaving patterned areas uncovered by amorphous LAO. A second deposition of a thicker epitaxial LAO film (> 4 u.c.) was performed and conducting paths were formed only where the amorphous film had been removed by the lift-off process [43]. Structures down to 200 *nm* could be produced using this method, but it requires two depositions of the LAO film at high temperature.

In another more recent approach, a hard AlO_x film was used as a lift-off layer. An amorphous AlO_x thin film was deposited by PLD on top of the STO substrate and patterned to a negative mask by photolithography and wet chemical etching [44]. The LAO film was deposited through the lift-off mask, which was then removed by an aqueous NaOH solution to obtain the final LAO structure (see Fig. 2.7). However, other groups reported that even the deposition of amorphous AlO_x on STO substrate can lead to the formation of a q2DEG at the interface and it is not clear what differences produce such discrepant result [45] [26] [46].

Finally another method proposed to pattern the LAO/STO interface without physical etching of the LAO film is by conducting tip atomic force microscope (AFM) writing. The method utilizes an electric field effect in a 3 u.c. non-conducting LAO/STO interface. Conducting paths could be written with very high precision down to a few nanometers by applying a local voltage using the AFM tip (see Fig. 2.8). The voltage of the tip would induce charge accumulation on the surface of the 3

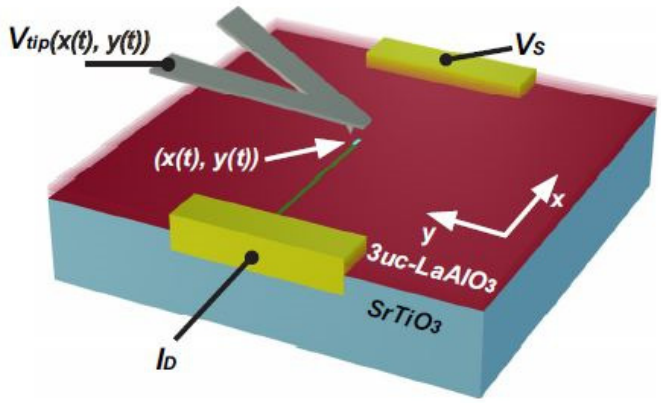

Figure 2.8 Graphical representation of the experimental setup to use an AFM tip to write conducting paths on an LAO/STO sample below the 4 u.c. critical thickness.(from *C. Cen, et al. Nature Materials, 2008.*)

u.c. LAO creating the condition for the formation of the q2DEG along the written paths; however it is important to comment that, because of the presence of water, the conductivity could be given by the hydrolyzed ions. Notwithstanding the nanometric resolution, this technique is difficult to scale up for fabrication of large area devices and show limited durability [47].

In our experiments we found that it is possible to use low-energy argon ion beam irradiation to permanently eliminate the conductivity in the LAO/STO interface without etching the LAO film physically. At low enough ion beam dose and energy, oxygen vacancies in the STO substrate are not formed. Combining this effect with electron beam lithography, nanostructures with dimensions down to 50 *nm* can be reliably fabricated.

3 Epitaxial growth of thin films

In this chapter we will describe the process and important parameters used for the deposition of thin films, in order to obtain the LAO/STO interfacial q2DEG.

3.1 Pulsed laser deposition

The interface is obtained by epitaxial growth of LAO film on a (100) TiO_2 terminated single crystal STO substrate.

To obtain a single TiO_2 termination, the STO substrate undergoes a cleaning and chemical etching, followed by a high temperature oxygen annealing; this process ensures the surface to be TiO_2 terminated [48], a condition required for the q2DEG formation. The LAO film is epitaxially grown, on such surface terminated STO substrate, by pulsed laser deposition (PLD). Epitaxial growth means that the film inherits the crystal orientation of the substrate template. In this way single crystal thin films of very high quality can be obtained. To ensure epitaxial growth, high temperature and high oxygen pressure should be provided during deposition [3]. In PLD a pulsed laser beam is focused by a lens on a target material surface; if the laser energy is high enough, it is sufficient to ablate material from the surface without heating of the target. This is a central property of the PLD as it ensures homogeneous ablation of all elements. Otherwise, evaporation rate is proportional to the melting temperatures of different composites. The ablated material leaves the target at a

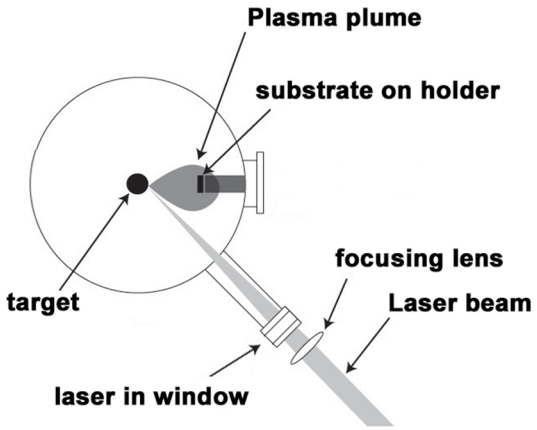

Figure 3.1 Schematic representation of the pulsed laser deposition (PLD) system.

normal to its surface forming a so called laser *plume* [48]. The target is made from a single crystal LAO; It is important to scan the laser beam by, *e.g.* target rotation, to avoid formation of an etched trace that can cause an uneven surface and deviation of the plume direction from the surface normal. The ablated material travels towards the substrate that is mounted at a fixed distance, facing the target and perpendicular to the plume direction (see Fig. 3.1). The substrate is mounted on a heater, which can be used to achieve the high temperatures required to obtain an epitaxial growth.

The deposition process can be performed in vacuum or by introducing a desired gas at a certain pressure in the vacuum chamber; this gas pressure can be used both to modify the plume profile and to regulate the stoichiometry of the deposition. The temperature of the substrate, the distance between substrate and the target, and the pressure inside the chamber are fundamental parameters for the result of the deposition. Our depositions are performed in oxygen atmosphere ($\sim 10^{-4} mbar$), with 5 *cm* distance between substrate and target and heating the substrate up to 800 °*C*. The thickness of the deposited film is also strongly dependent on the position of the substrate respect to the plume, but the use of small substrates (5×5 mm^2 in our case), ensures a very uniform deposition along the entire surface.

3.2 Real time monitoring of film growth using RHEED

The growth of the film can be monitored *in situ* in real time by reflection high-energy electron diffraction (RHEED) [49]. An electron gun generates a beam of electrons which is directed on the surface of the sample at a very small angle of incidence. Incident electrons are scattered from atoms at the surface of the sample, and a small fraction of the scattered electrons interfere constructively at specific angles and form regular diffraction patterns on a phosphor screen used as detector. The electrons

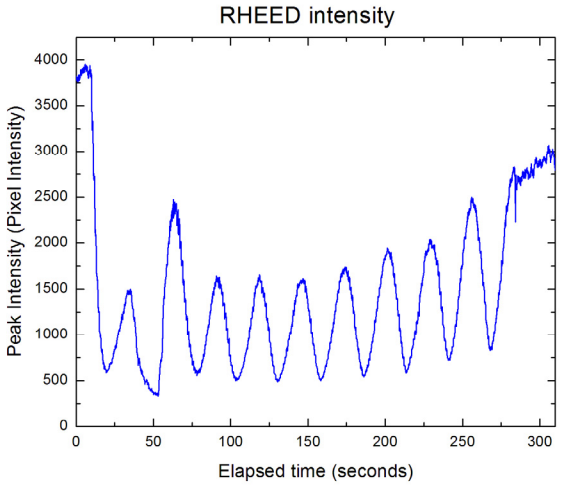

Figure 3.2 Reflection high-energy electron diffraction (RHEED) peaks of intensity as a function of the elapsed deposition time; the number of maxima in the plot corresponds to exactly 10 u.c. of LAO deposited. (The beam current was increased after 1.5 unit cells deposited).

interfere according to the position of atoms on the sample surface, so the diffraction pattern at the detector is a function of the sample surface. The specific angles of constructive interference for the diffracted electrons depend on the crystal structure and spacing of the atoms at the sample surface, and on the wavelength of the incident electrons. During the deposition, the presence of material in random positions on the surface creates a roughness that scatters the reflection reducing the intensity of the constructive interference. When a full u.c. layer is deposited, the interference peak shows an intensity maximum (see Fig. 3.2); counting these maxima, it is possible to know the exact number of u.c. layers deposited. As indicated before, at least 4 u.c. of LAO are required to form the q2DEG at the LAO/STO interface; however, a choice of depositing exactly 4 u.c. may result in non-homogeneity in the q2DEG due to local variations in the film thickness along the sample area. For this reason a standard thickness of 10 u.c. of LAO was used in our samples. For all samples discussed in this work the RHEED monitoring showed clear intensity oscillations confirming a layer-by-layer growth. Immediately after the deposition, the samples were annealed for 1 hour at 600 $°C$ and 500 *mbar* of oxygen. After the deposition process, all the samples were inspected in atomic force microscope (AFM, Bruker Dimension ICON) to confirm the smoothness of the surfaces and the presence of 1 u.c. step terraces.

In the case of the samples with the SCO capping layer, more deposition steps are required, including deposition of 6 u.c. of LAO on top of the TiO_2 terminated STO substrate. Then 1 u.c. of SCO is deposited from a sintered powder $SrCuO_2$ target. Finally two u.c. of STO are deposited, from a single crystal STO target, to protect the surface of the sample from chemical interactions. The SCO capped samples discussed in this thesis are (if not specified otherwise) not post-annealed to follow the procedure reported in [30]. Depositing only 6 u.c. of LAO ensures that the film thickness is above the threshold reported in [30] but at the same time the total thickness of the STO/SCO/LAO multilayer stack (2+1+6=9 u.c.) is comparable to the one of the 10 u.c. LAO. This is important, as we will see later, to compare the results obtained with the irradiation on the capped and non-capped samples.

4 Metal-insulating transition by low Ar ion irradiation

The first part of this work was devoted to find a suitable way to pattern the q2DEG at the LAO/STO interface. A reliable and robust technique for nano-patterning of the LAO/STO interface is required for practical device fabrication, as well as for understanding of the nature of the electron gas on the nanoscale. In our experiments we found that it is possible to use low-energy argon ion beam irradiation to permanently eliminate the conductivity in the LAO/STO interface without etching the LAO film physically. In this chapter we describe the effect of the low energy irradiation on the LAO/STO film, and we discuss the mechanism of the induced metal-insulator transition (MIT).

4.1 Low energy Argon ion irradiation of the LAO/STO interface

The basic idea of our experiment was to find possible conditions to etch the LAO/STO film without producing oxygen vacancies in the STO substrate. First of all, we performed a measurement of the electrical resistivity of the q2DEG, *in situ* during the Ar^+ irradiation, as a function of beam energy and dose.

The irradiations were performed in an Oxford IonFab 300 Plus system using an inductively coupled Ar^+ plasma source (3 *cm* beam aperture). The sample is mounted

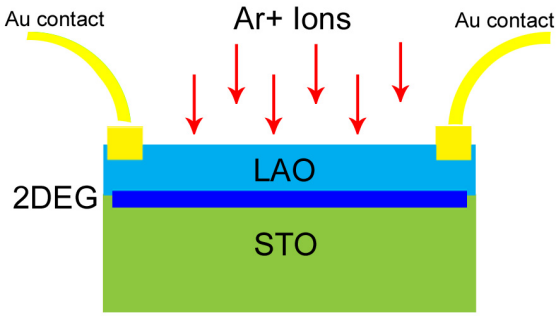

Figure 4.1 Schematical representation of the experimental setup for the *in situ* measurements of electrical conductivity during the Ar irradiation.

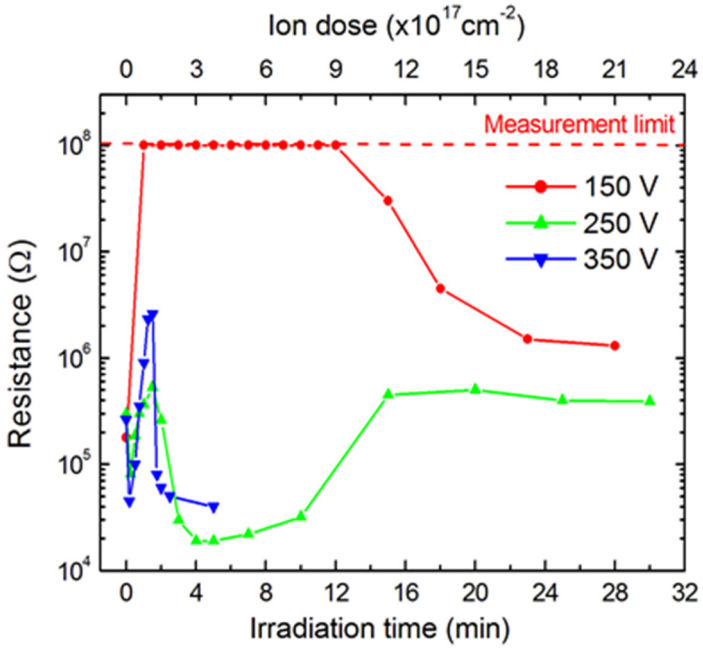

Figure 4.2 Resistance of 10 u.c. thick LAO/STO as a function of the irradiation time (ion dose) measured *in situ* during ion beam irradiation for three different values of energy of the ion beam and an incident angle of 30°.

on a rotating stage to ensure a more uniform irradiation. Beam energy and the irradiation time were used as adjustable parameters. Another tunable parameter during the Ar^+ irradiation is the angle between the ion beam and the normal to the surface of the LAO/STO sample; in most experiments, 30° angle was used, but in some cases 0° was also used. The effect of angle will be discussed later. The electrical transport properties were measured *in situ* in a 4-point van der Pauw configuration.

Three different 10 u.c. thick LAO/STO samples were irradiated and the electrical resistance of these samples was measured *in situ* as a function of Ar^+ ion irradiation dose for three different beam voltages of 150, 250, and 350 V. A constant beam current density of 0.14 mA/cm^2 was used corresponding to a dose rate of 9×10^{14} Ar^+/cm^2s) (this value will be the one used for all the irradiation discussed in this thesis, unless otherwise specified).

The resistance rapidly increases in the beginning of the irradiation for all samples, see Fig. 4.2.[1] For the 150 V beam voltage, the resistance becomes immeasurable (R > 200 GΩ, measurement limit) after about 1-2 min (corresponding to an ion dose about 1×10^{17} Ar^+/cm^2). For higher beam energies, the resistance initially increases, but instead of reaching the measurements limit it saturates at lower value than before irradiation. This suggests that the ion irradiation creates oxygen vacancies in the STO substrate. It is well known that oxygen vacancies donate

[1] In Fig. 4.2 it is actually possible to see a small decrease of the resistance before the rapid increase we are interested in. This decrease can be explained by the accumulation of charges on the sample as we start the irradiation.

electrons in the conducting band of the STO which results in n-doping [50]. The electron doping due to oxygen vacancies decreases the electrical resistance after longer irradiation times. In the case of 150 V beam energy, it takes much longer time for the electrical conductivity to appear again and this leaves a time interval where the irradiation can be stopped leaving the interface in an insulating state. Therefore, a 150 V beam irradiation of suitable duration (around 5 minutes) can be used to induce a metal-insulator transition (MIT) at the LAO/STO interface. The induced MIT showed a remarkable stability and durability over several months (even years) from the irradiation.

4.2 Simulation of ion induced damage

Ion induced damage during Ar^+ irradiation in the LAO/STO heterostructures was simulated using the Stopping and Range of Ions in Matter (SRIM) software [51]. Irradiation conditions similar to ones used in experiment (Ar^+ ions, 30° incident angle, number of ions corresponding to the dose rates used in the experiment) were used in the simulations. The results of the simulations are shown in Fig. 4.3. 150 eV Ar^+ ions are effectively stopped by the 10 u.c. thick LAO film, and therefore do not reach the interface at least in the beginning of the irradiation process (actual etching of the LAO film was neglected in the simulations). The penetration depth of ions increases at higher beam voltages and the beam trajectories start to reach the STO substrate. This suggests that the observed behavior of the electrical resistance in our

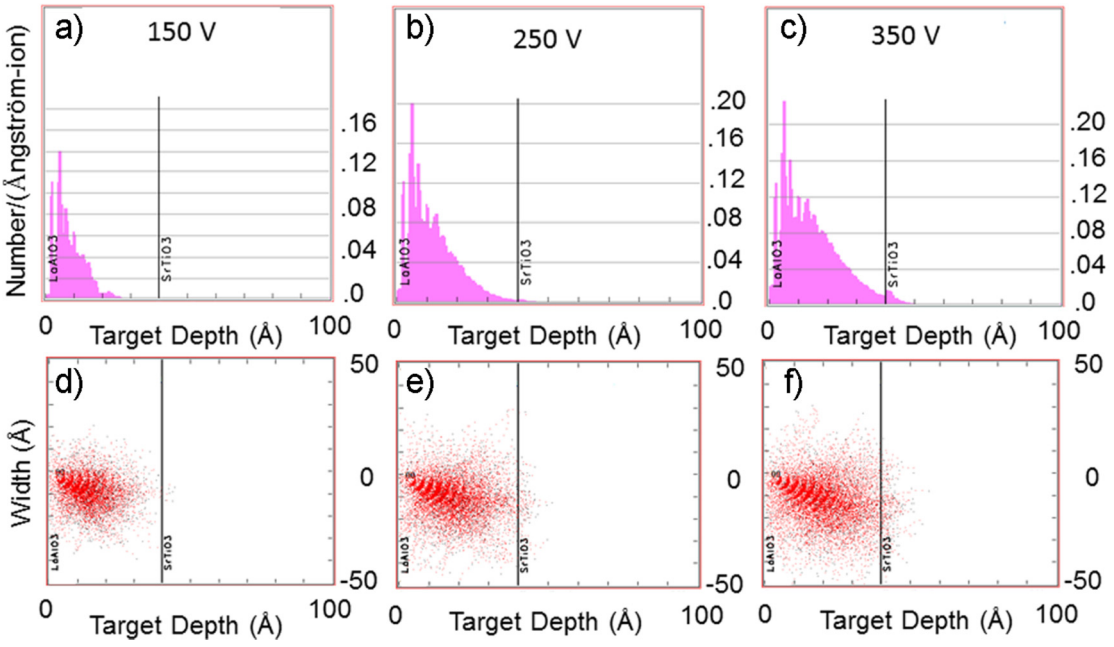

Figure 4.3 Stopping and Range of Ions in Matter (SRIM) simulation results for a 30° angle incident beam, and number of ions per unit cell corresponding to the ion dose in the experiment. On top, number of oxygen vacancies formed by the incident ions as a function of depth into the LAO film for different beam voltages, nominally a) 150 V, b) 250 V and c) 350 V. On bottom penetration depth of the Ar ions in the LAO film for different beam voltages, nominally d) 150 V, e) 250 V and f) 350 V.

experiments with higher beam voltages can be related to the formation of oxygen vacancies in the STO layer. This is further supported by the simulations of oxygen vacancies produced by incident ions in the LAO/STO heterostructures at different beam voltages (see Fig. 4.3, (a), (b) and (c)). At low energies, the effect of the ion damage on oxygen in the STO substrate is negligible, in agreement with our experimental results. At higher beam voltages, oxygen vacancies are formed already in the beginning of the irradiation process and this causes a rapid decrease in the electrical resistance of the sample. It is important to note that the simulations do not take into account the possible physical etching of the LAO layer during the irradiation process. For the low energy beam, the formation of oxygen vacancies in the STO substrate requires much higher doses (up to 10^{18} Ar^{+}/cm^{2}) due to the slow etching (almost neglectable as we showed) and thus provides a suitable time interval for the patterning of a conducting interface in the LAO/STO.

4.3 Effects of LAO film thickness on ion irradiation

We also investigated the time dependence of the resistance variation during low energy ion beam irradiation for samples with different LAO film thickness. Three samples with different thickness, nominally 5, 10 and 15 u.c., were irradiated under similar conditions as described above at 150 eV beam voltage, 30° incident beam, and their resistance was measured as a function of irradiation time *in situ*. The results are reported in Fig. 4.4. The measurement shows that the time required to reach the insulating state increases with the film thickness; conductivity disappears after only 1 min of irradiation in the 5 u.c. thick film, after 2 min for 10 u.c. thick film, and after 10 min for 15 u.c. thick film. The dependence of the irradiation time required to

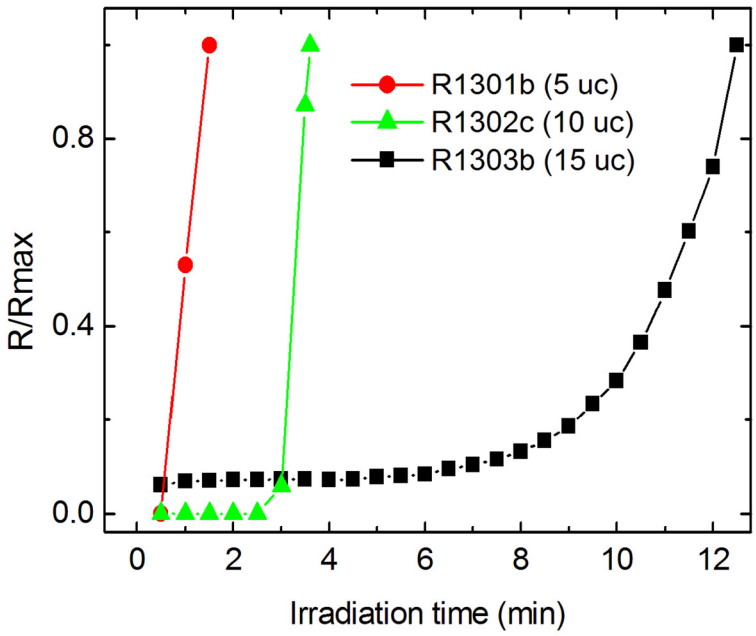

Figure 4.4 *In situ* measured resistance (normalized at the maximum value) as function of irradiation time for different LAO film thicknesses, *i.e.* 5, 10 and 15 u.c. The dose rate is 9×10^{14} Ar^{+}/cm^{2} *s*.

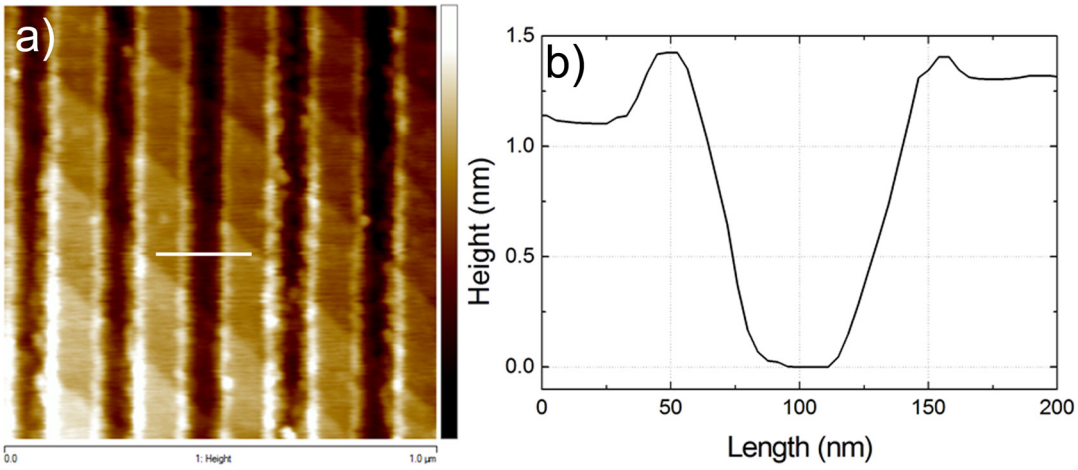

Figure 4.5 a) Atomic force microscope (AFM) image of a sample patterned with 100 *nm* linewidth non-irradiated lines (bright ones) spaced by 100 *nm* irradiated areas (dark ones), and b) profile height of the patterned lines corresponding to the white section in a).

induce the metal-insulator transition (MIT) on the LAO film thickness, shows that the conductivity at the interface is not removed as soon as the Ar^+ ions interact with the LAO surface. The longer the irradiation the deeper will be the penetration of the Ar^+ ions into the LAO/STO, so this experiment shows that Ar ions are required to reach some depth into the LAO film in order to destroy the conductivity. It is however impossible to estimate how deep the ions need to penetrate into the LAO film, because of the other effect induced in the film by the irradiation, *i.e.* the film is partially etched (the effective thickness is reduced) and partially amorphized (density and penetration rate of the ions change).

Finally we studied the effect of the irradiation on SCO capped LAO/STO samples. As discussed, the total thickness of the LAO/STO interface with capping layer was 9 u.c. (6 u.c. LAO+1 u.c. SCO + 2 u.c. STO). Irradiation experiment confirmed that irradiation time required to eliminate conductivity at the SCO capped interface is the same as for uncapped LAO/STO 10 u.c. thick (around 1 min, with the same voltage and dose).

4.4 The role of incidence beam angle during Ar^+ irradiation

It has been shown that a low energy Ar irradiation can induce a MIT at the LAO/STO interface, however further investigation is required to understand the mechanism of such a transition.

A simple reason of the MIT would be that the LAO film is physically etched so its thickness becomes smaller than the 4 u.c. that is required for the formation of the conducting interface. To investigate this possibility we analyzed irradiated samples with atomic force microscope (AFM).

Two regular patterns consisting of 100 *nm* (50 *nm*) wide conductive lines separated by 100 *nm* (50 *nm*) wide insulating lines were fabricated from 10 u.c. LAO sample using electron beam lithography and low-energy Ar^+ ion beam irradiation. The AFM images of the structures (see Fig. 4.5) show that the height difference

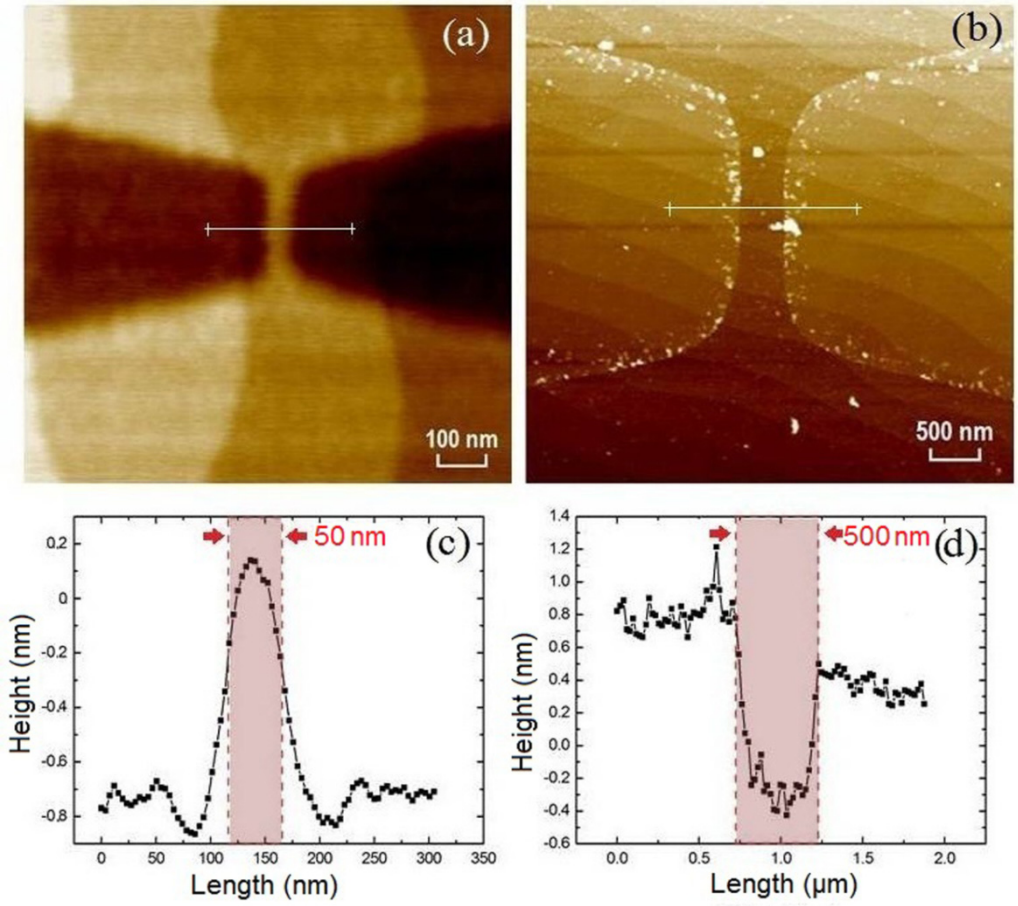

Figure 4.6 AFM imaging of bridge structures (top), and relative profile height (bottom); the structures were patterned using 30° incident beam in a) and c), or 0° incident beam in b) and d). The shaded areas in c) and d) represent the expected size of the bridges (hence the non-irradiated regions)

between irradiated and non-irradiated lines is around 1 *nm*. This proves that the LAO film thickness after irradiation is reduced by no more than 2-3 u.c. (1 u.c. corresponds to a thickness of about 0.4 *nm*).

To further prove that irradiation does not result in a significant etching of the film, several structures were irradiated at 0° incidence angle. The low incidence angle is known to result in lower etching rates [52]. AFM images of two structures patterned with 30° and 0° angle incident beam are reported in Fig. 4.6a and 4.6b, respectively. The step height in Fig. 4.6a (for 30° incidence angle) corresponds well to the previous sample showed in Fig. 4.5. In Fig. 4.6b the step is inverted and the irradiated areas appear higher than non-irradiated ones. This effect can be explained considering that irradiated part of the LAO film may be amorphized, causing an effective "swelling" of the film [53].

These experimental observations clearly prove that irradiation does not reduce LAO film thickness below critical value and therefore this cannot be a cause for the MIT.

4.5 Crystallinity of the film after irradiation

High crystalline quality of the LAO film is expected to be crucial for the formation of the q2DEG. Ion beam irradiation may strongly affect crystalline properties of the film through partial amorphization or creation of various defects, and this may be a possible reason of the MIT. To study this possibility, irradiated samples were investigated with scanning transmission electron microscope (STEM).

The STEM is a special type of transmission electron microscope (TEM) in which the electron beam is focused into a narrow spot that is then scanned over the sample; this makes the STEM suitable for analysis techniques such as energy dispersive X-ray spectroscopy (EDS), electron energy loss spectroscopy (EELS) and annular dark-field imaging (ADF).

Fig. 4.7 shows STEM images from a sample with 50 *nm* lines (as described in previous section). The cross-section of the sample is made in a direction perpendicular to the patterned lines, so it is possible to see a boundary between the irradiated and non-irradiated areas. The images show that the boundary between the two areas is very sharp, about 5 *nm* compared with line width of 50 *nm*. The thickness of the crystalline part in irradiated areas is about 5-6 u.c., corresponding well with observation made by AFM regarding the etching rate. Moreover, the crystalline quality of the LAO film in both the irradiated and non-irradiated areas is not distinguishable and no defects were found in the irradiated parts that are not present in non-irradiated ones. This clearly demonstrates that irradiation does not destroy the crystallinity below 4 u.c.; however STEM does not provide information about the point defects that may be created during irradiation, and cause the MIT.

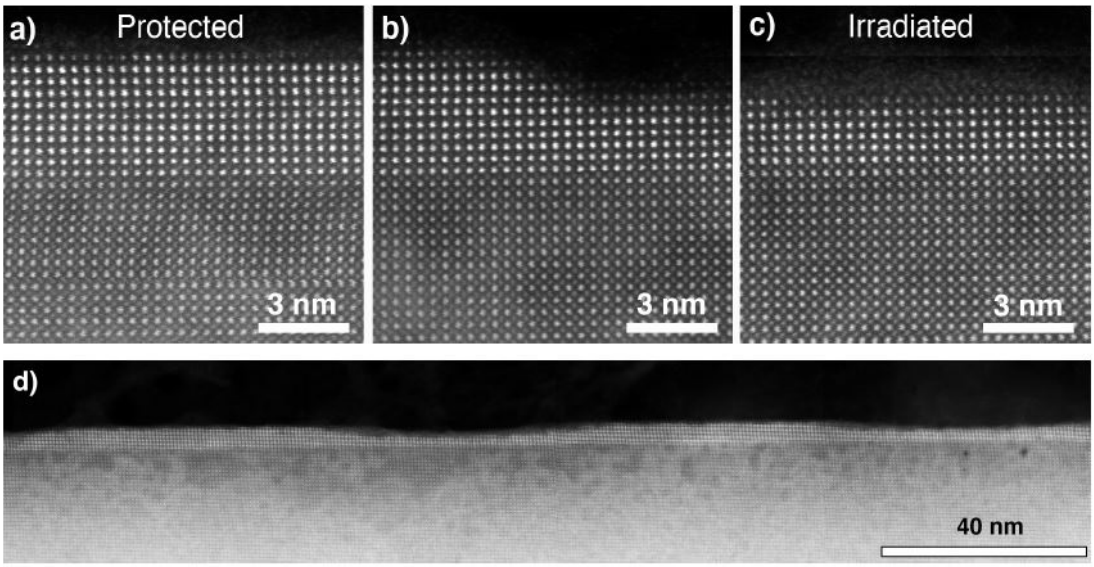

Figure 4.7 Scanning transmission electron microscope (STEM) crossection images of the patterned LAO film on an STO substrate. a) shows a protected area where all the initial 10 u.c. are visible c) shows an irradiated area where 5-6 u.c. are still crystalline and b) shows an edge between the two areas. d) shows an overview of the patterned sample, where several irradiated regions are visible.

4.6 Reversibility of the metal-insulator transition

STEM imaging showed that the LAO film crystallinity is not evidently affected by irradiation. Still, point defects such as La^{3+} on Sr^{2+} replacements or cation vacancies may be created that are not easily detected in STEM. If this is the case, high-thermal annealing may result in diffusive recovery of the film crystallinity, and restore the original film properties. Therefore, several annealing experiments were performed under controlled environment and with *in situ* RHEED imaging.

For the experiments, after the deposition of the LAO film, each 5×5 mm^2 sample was cut into two pieces of 5×2.5 mm^2. This allowed us to compare samples that had identical initial state, before and after irradiation and post-annealing. One of the two halves was irradiated by low-energy Ar^+ ions for 5 minutes. The conductivity of the samples was measured with four-point contacts in a van der Pauw configuration. As expected, the irradiated half showed completely insulating behavior (R > 200 GΩ, our experimental setup measurement limit). The non-irradiated sample was metallic with values of $R_s \approx 10^5\ \Omega/\square$ and $n_s \approx 1.5 \times 10^{13} cm^{-2}$ at room temperature, characteristic for the LAO/STO interface.

One of the irradiated samples was then annealed at 10^{-4} *mbar* of oxygen partial pressure, and the process was monitored using *in situ* RHEED [49]. Fig. 4.8 shows a series of RHEED images during this annealing process. At the beginning of the process, when the sample is at room temperature, no RHEED pattern is seen, implying that the surface of the LAO is in an amorphous state. As the temperature increases it is possible to notice that the recrystallization process begins at around 500 *°C*; at 600 *°C* the RHEED image is completely identical to the one corresponding to a

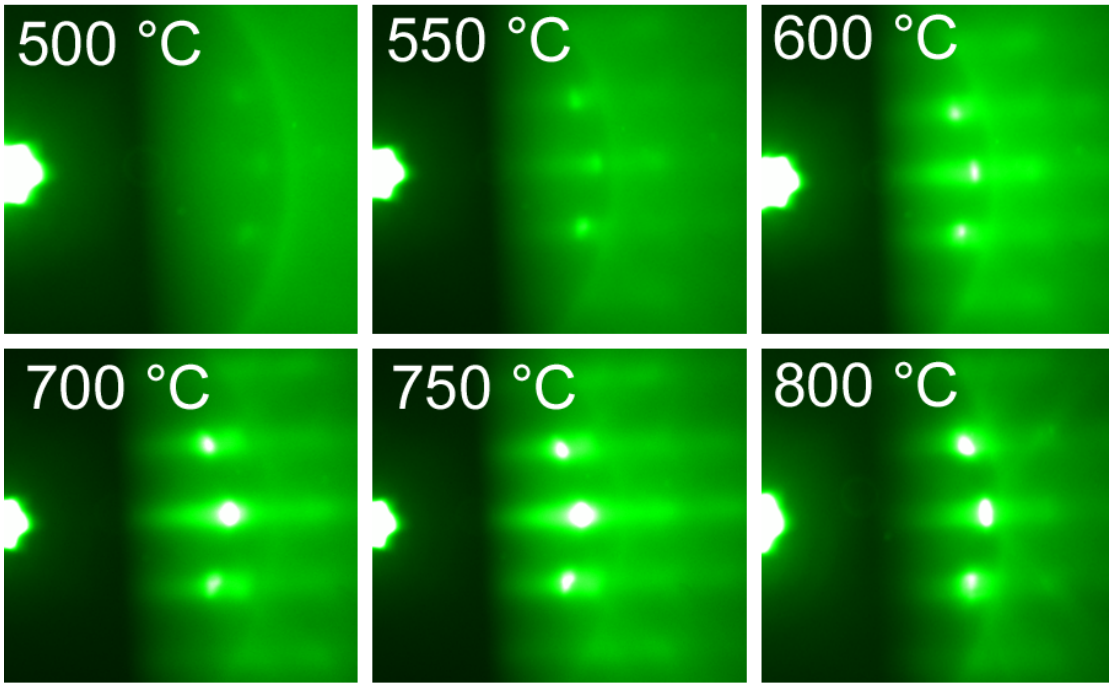

Figure 4.8 RHEED interference peaks for the irradiated sample at several temperatures during the post-annealing process. It is possible to see that the recrystallization starts around 500 *°C* and is complete around 600 *°C*, after that there are not noticeable differences up to 800 *°C*.

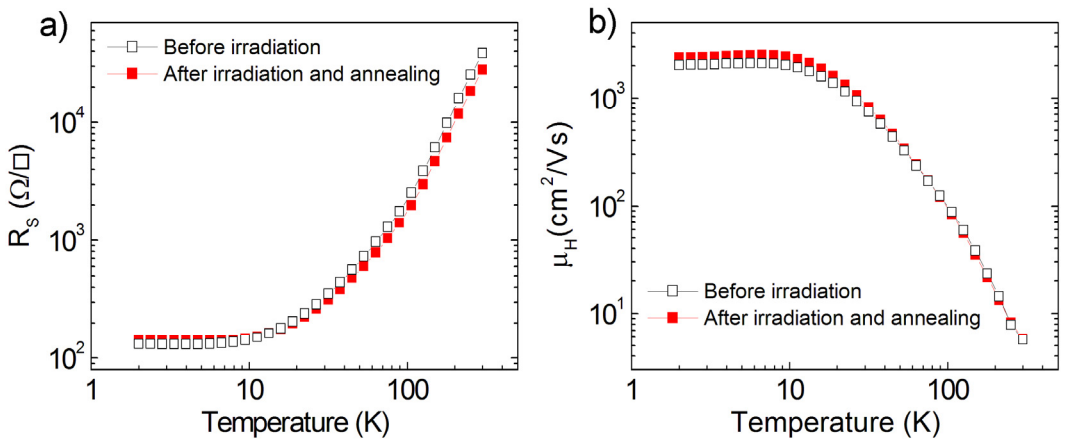

Figure 4.9 Temperature dependence of the a) sheet resistance and b) charge mobility for the LAO/STO sample just after the interface deposition (empty squares) compared to the one after irradiation and re-annealing at 800 °*C* (full squares). The irradiated sample is restored to a state with nearly identical electrical properties to the initial one.

sample just after the deposition, indicating that the recrystallization is already complete. For further increase of the temperature, it is possible to notice that the RHEED pattern does not significantly change between 600 °*C* and 800 °*C*. After reaching 800 °*C*, the sample was kept for 15 minutes at this temperature then cooled to room temp at the same pressure.

The irradiated sample that was post-annealed for 15 minutes at 800 °*C* and 10^{-4} *mbar* O_2 showed, after the treatment, metallic behavior with conductivity and carrier concentration very similar to a non-irradiated one. The temperature dependencies of sheet resistance, electrical mobility and carrier density, for the sample that was irradiated and annealed at 800 °*C* (with post-annealing at 600 °*C*, 500 *mbar* O_2) is compared to the one for the non-irradiated sample in Fig. 4.9. The resistivity of the irradiated annealed sample at room temperature is slightly lower than in the non-irradiated one, but shows an upturn at low temperature below 10 *K*. This may be due to the fact that the thickness of the sample is slightly reduced after irradiation, as discussed in previous sections.

To investigate the effect of the oxygen pressure during the post annealing of irradiated samples, different oxygen pressure was used for annealing at 800 °*C*, in the range from 10^{-4} *mbar* up to 10^{-1} *mbar* O_2. In every case, the annealing at 800 °*C* was followed by an additional annealing step for 1 hour, 600 °*C* and 500 *mbar* O_2. In all the samples, the conductivity was restored to the metallic state (comparable to the state before irradiation) independently from the oxygen partial pressure used.

We thus demonstrate that electrical conductivity in insulating irradiated samples can be completely restored to the initial state by annealing at 800 °*C* and that it survives post-annealing in oxygen atmosphere.

4.7 Argon implantation in the LAO/STO

In order to find a structural origin of this reversible MIT, XPS was used to study sample composition before irradiation, after irradiation and after post-annealing. XPS

is a quantitative spectroscopic technique that measures the elemental composition of a material. It is the most widely used surface analysis technique because it can be applied to a broad range of materials. XPS is surface-sensitive technique; spectra are obtained by irradiating a material with a beam of X-rays while simultaneously measuring the kinetic energy and number of electrons that escape from the top 10 *nm* of the material. This technique detects only those electrons that have escaped from the sample and reach the detector through the vacuum of the instrument. Photo-emitted electrons can undergo inelastic collisions, recombination, excitation of the sample, recapture or trapping in various excited states within the material, reducing the effective number of escaping photoelectrons. The probability of such effects creates an exponential attenuation as a function of the depth, making the signals from the surface much stronger than the signals from deeper layers.

The XPS studies were performed at the Department of Material Sciences, Technical University of Darmstadt, Germany. The XPS investigations indicate that all the irradiated samples show presence of Ar in the sample, which are, of course, never reported in as-deposited samples. No presence of Ar is found in sample annealed at 800 °*C* (conductive sample). Thus all conductive samples (before and after irradiation) show no presence of Ar.

The XPS data combined with the observation reported in previous paragraphs indicate that the MIT may be related to Ar implantation. During the irradiation Ar ions can be implanted into the LAO film. These Ar ions can create defects that destroy conductivity at the interface. It is still not clear what it is the exact mechanism that relates the defects to the MIT. We can infer that the defects act as traps attracting electron, or that they modify the effective field. The density of Ar ions implanted estimated from the dose corresponds well to the electron density of the q2DEG. The Ar defects are stable at room temperature, but high temperature post annealing (800 °C) gives enough energy to the implanted Ar to make them diffuse away from the LAO film restoring the condition required for the formation of the q2DEG. This is a very plausible scenario that can explain all experimental findings related to Ar ion beam irradiation and corresponding MIT in the LAO/STO.

5 Patterning of the LAO/STO interface

We showed in the previous chapter that it is possible to induce a metal-insulator transition (MIT) at the LAO/STO interface by using low energy Ar ion irradiation. In this chapter we will describe, in detail, how the irradiation can be used in conjunction with optical or e-beam lithography to pattern structures down to the nanoscale into the q2DEG. In the last paragraph we will describe the structures that we patterned with this technique.

5.1 Lithographic techniques

The first step in order to pattern the q2DEG at the LAO/STO interface is to create a resist mask to cover areas that we want to be protected by irradiation. This mask can be obtained through optical or e-beam lithography.

Optical lithography (also called photolithography) is a technique that uses an ultra-violet (UV) light source (in our case 365 *nm* wavelength) to transfer a pattern from a hard mask (e.g., a thin film chrome pattern on a quartz substrate) to the sample. First of all, the sample is coated with a liquid solution of photoresist through spinning. The speed and acceleration of the spinning will regulate the thickness of the photoresist layer. The photo resist-coated sample is then prebaked on a hotplate to evaporate excess photoresist solvent. The hard mask is then put in contact with the coated surface of the sample to select areas to expose, and the photoresist is then exposed to intense UV light (nominally 6 mW/cm^2). The exposure to light produces a chemical change in the photoresist that allows the exposed parts to be removed by a special solution called developer. The photoresist is commonly called positive if the exposed area becomes soluble in the developer; there are also negative photoresists, where the unexposed regions are the ones soluble in the developer. In our case we used a positive resist called S1813. The photolithography minimum resolution is limited by optical diffraction, for this reason the smallest structure we can obtain with our UV source is in the order of 500 *nm*.

To pattern smaller structures e-beam lithography is required. The e-beam lithography is a technique that uses a focused electron beam to expose a polymer resist coated sample. The sample is coated in a similar way as described for optical lithography, but with an electron sensitive resist. The main advantage of the e-beam is that the electron beam is scanned over the sample allowing to direct-write custom

patterns with resolution down to 10 *nm*. The resolution is however limited by other factors such as the quality of the resist, beam energy used, back- and side-scattered electrons, and sample properties (reflectivity, electrical conductivity, etc.). In our case we used a negative resist called maN2401. The instrument used for our experiments is a JEOL JBX-9300FS that can be used with 50 kV or 100 kV acceleration voltages. The time required for a complete exposure depends on the doses used, but at the same time for smaller beam currents, a better resolution can be achieved. For this reason e-beam exposure is often split in different steps, where smaller features are exposed with lower beam current. The different exposures are always aligned thanks to cross-marks on the sample (usually drawn by photolithography). In the same way as in the photolithography case, the resist is then developed to obtain the final mask.

5.2 Patterning of the q2DEG

Once the resist mask is obtained thanks to optical or e-beam lithography, we can use the low energy Ar^+ irradiation to draw structures in the q2DEG at the LAO/STO interface. Irradiation of the sample will induce the metal-insulator transition (MIT) in unprotected areas (see Fig. 5.1) as described in Chapter 4. The resist protected areas, on the other hand, will not be affected by the irradiation, and thus conducting paths will be formed. This technique allows to pattern structures in the q2DEG, whose dimension are limited only by the resolution of the resist, in our case 500 *nm* for the optical lithography and 50 *nm* for the e-beam [52]. Examples of structures patterned with our technique were already reported in Chapter 4, and the electrical characterization of specific structures will be described in Chapter 6.

It is important to note that our patterning technique solve most of the problems connected to other existing techniques, described in Chapter 2. This technique allows patterning of the q2DEG without physically etching the LAO film, hence never exposing the interface to external environment after the *in situ* deposition of the LAO film and capping layer. We avoid the use of aggressive chemicals, and only one deposition step is required. Our technique creates a durable patterning in the q2DEG:

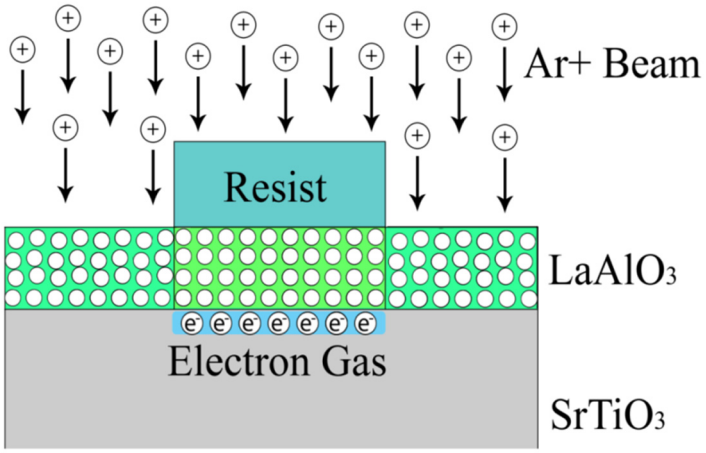

Figure 5.1 Illustration of the patterning technique using low energy Ar ion irradiation. The resist layer protects the q2DEG that is otherwise destroyed in non-protected areas.

the induced MIT is stable in time. The results reported in this work are the product of several measurements repeated over a span of 2-3 years, and no change in electrical properties was found over such a long period of time in any of the samples. The resolution (50 *nm*) is one of the best reported (except AFM writing) and in the present state we can assume it is only limited by the resist resolution, therefore it can be further improved by refining the e-beam lithography. Moreover thanks to the combination of Ar ion irradiation and lithography, this technique is easily scalable over larger areas of the sample.

5.3 Patterned structures

The first structures we pattern on our samples are macroscopic Hall bars of 30 µm width and 200 µm length. On each of our samples there are always at least three of those Hall bars with different angles in respect to crystallographic axes of the sample (usually 0°, 45° and 90°). These structures are used to check overall quality of the sample q2DEG and, as we will see later, to compare macroscopic electrical properties to the ones on nanoscale.

Then we fabricated samples with micro- and nano-bridges. The bridges have several widths, starting from 1 µm and going down to 50 *nm*. The length of the bridges changes accordingly, in order to always keep the same length-to-width ratio (nominally 5:1), so it is easier to compare the sheet resistance of the structures. All the bridges are contacted through a four-point configuration. The purpose of those structures is to study the electrical properties as function of decreasing dimensions.

After this we fabricated samples with nano-Hall bars and nanorings. The nano Hall bars have all 100 *nm* widths but different lengths (nominally 200, 400 and 700 *nm*). They have also different orientations with respect to the substrate crystallographic axis, as well as the macroscopic Hall bars described earlier. The

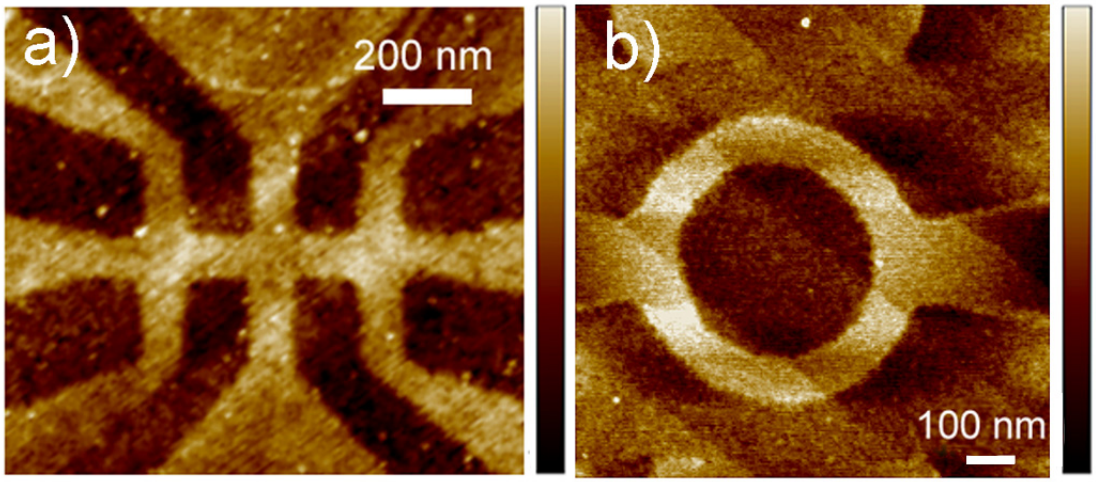

Figure 5.2 AFM height images of two nanostructures patterned in the SCO-capped LAO/STO interface using Ar+ ion beam irradiation: a) Hall bar with nominal linewidth of 100 *nm* and segment length of 200 *nm*, and b) Ring with nominal linewidth of 100 *nm* and inner diameter of 400 *nm*. In both figures the color scale ranges between -1 *nm* and 1 *nm*.

nanorings have line width W from 300 *nm* down to 50 *nm* and inner diameter D proportional to the width (nominally $D = 4 \times W$). All the nanorings are contacted through a four-point configuration. The structures were analyzed with atomic force microscope (AFM) to verify the correspondence between expected and effective dimensions. Examples of these AFM images can be seen in Fig. 5.2. The nano-Hall bars are patterned on our samples to obtain sheet resistance, charge mobility and carrier density of the nanoscale structures and to compare them with the ones at macroscale.

5.4 Cleaning of the LAO/STO surface

As discussed in earlier chapters, to form the electron gas at the LAO/STO interface, at least 4 u.c. of LAO are required, corresponding to a critical thickness of approximately 1.6 *nm*. The proximity of the electron gas to the surface creates a strong coupling between the electrical properties of the q2DEG and surface polar adsorbates [47] [54] [55]. Furthermore, it has been found that commonly used solvents, such as acetone, negatively affect the transport properties of the interface if adsorbed on the LAO surface [55]. Therefore, in order to retain the transport properties of the LAO/STO interface as-grown, it is important to remove or passivate the surface adsorbates.

In the latest years has been suggested also the possibility to integrate the LAO/STO interface with other materials such as graphene [56]. In order to deposit other materials on top of the LAO/STO, an adsorbate-free surface is a key point, especially after the processing steps required for the patterning (etching and lithography). We discussed how the formation of the electron gas at the LAO/STO interface is strongly affected by oxygen vacancies [25]. Moreover we showed in the last chapter that the interface is sensitive to ion irradiation that can cause a metal-insulator transition. For these reasons we have to face restrictions on the use of oxygen, heat, and plasmas in treating the samples.

In an experiment complementary to the main project presented in this thesis, we found that an UV/ozone irradiation can produce a very clean surface without any etching and, at the same time, can improve the electrical transport properties of contaminated samples. In this way we were able to partially restore the properties of the treated samples (patterning etc.) to the as-grown ones.

Ultraviolet light produced ozone and irradiation (UV/ozone) is a relatively harmless and routinely used method to remove contaminants from surfaces [57]. In this method, UV light dissociates oxygen gas to atomic oxygen, which in turn forms ozone. The UV light also excites contaminant molecules on the surface and dissociates them, forming free radicals. The free radicals and excited molecules interact with the ozone and atomic oxygen to form volatile molecules which leave the surface, causing a cleaning effect. The main advantages of the UV/ozone method are that there is no heating (except from the UV light) and no energetic particle bombardment of the surface. These properties are crucial for samples which are sensitive to, e.g., annealing or etching.

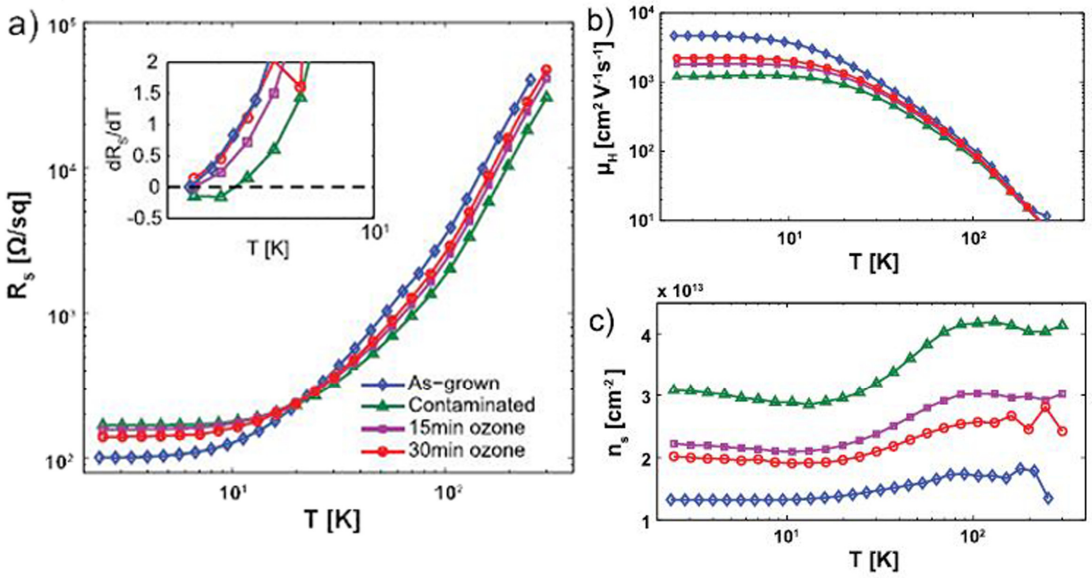

Figure 5.3 Electronic transport characterization of the LAO/STO interface after growth (blue open diamonds), contamination of the free LAO surface by exposed and developed photoresist (green open triangles), 15 min of UV/ozone (purple open squares), and 30 min of UV/ozone (red open circles). Temperature dependence of a) sheet resistance, b) Hall mobility, and c) sheet carrier density. The inset in a) shows the temperature derivative of the sheet resistance. Note the change of sign of the derivative for the contaminated sample. Also note that by contaminating the surface with photoresist, there was a considerable change of the sheet resistance, mobility and sheet carrier density. These changes could be partially counteracted by the UV/ozone cleaning.

The effect of the UV/ozone method on the electrical transport properties of the processed LAO/STO interfaces is summarized in Fig. 5.3. It is evident that the transport characteristics of the electron gas are affected by both the photolithography process and the UV/ozone cleaning. After growth, typical values for the conducting interface are sheet carrier density ≈ 1.5×10^{13} cm^2 and Hall mobility ≈ 5000 $cm^2V^{-1}s^{-1}$ at 2 K [7]. After the resist development, the sheet carrier density increases by a factor of 2 while the low temperature mobility decreases by a factor of 5. Therefore, the decrease in mobility cannot be explained just by the higher sheet carrier density but also by a change of scattering process. Note that the temperature dependent sheet resistance curves for samples with different sheet carrier densities cross at a temperature slightly above 20 K (see Fig. 5.3 (a)). Below this temperature, the sheet resistance increases with higher sheet carrier density. A similar effect has been seen in bare STO samples where the surface carrier density was varied by an electrolyte enhanced electric field [58]. The resistance increased with higher surface carrier density, and moreover, it had a Kondo type temperature dependence with a characteristic resistance upturn at low temperatures, similar to LAO/STO samples grown at high oxygen pressure [21].

The sheet carrier density of a 10 u.c. LAO/STO sample increased almost three times after the surface was exposed to polar solvents such as acetone or water, while

nonpolar solvents had almost no effect. We see a similar increase in the sheet carrier density, but in our case caused by the residual photoresist on the LAO surface. After the UV/ozone cleaning, there is a significant decrease in sheet carrier density, and also a decrease in its temperature dependent characteristics. Fifteen minutes is sufficient to reduce the negative effect of the photolithography process to approximately half, and an additional 15 min reduces the effect slightly more. The fact that the original transport properties could be partially restored indicates that the negative effects were due to the contamination layer.

5.5 Alternative application of the patterning technique

As we discussed the patterning technique we developed has a series of useful properties (resolution down to 50 *nm*, extremely durable samples, flat surface, scalability). Our technique can then be an important instrument for many other experiments related to the LAO/STO interface, and in parallel to the main PhD work we developed other side projects thanks to this powerful tool (such as nanoscale light sensors, intrinsic S-I-S junctions, etc.).

In a in collaboration with University of Naples and University of Rome, a terahertz (THz) experiment was performed using samples prepared by the Ar ion irradiation patterning technique at Chalmers. The goal of this experiment was to investigate how the low-temperature softening of the TO1 phonon of bulk STO can be hindered by ultrathin metallic films on its surface. The fabrication consisted in producing parallel conducting stripes spaced by insulating areas. Thanks to our techniques we were able to pattern 2.4 μm wide stripes, spaced by 1.6 μm, with a step of less than 1 *nm* over the full surface of a 5×5 mm^2 large sample(see Fig. 5.3). The THz reflectivity experiments were performed on different kinds of samples: bulk STO, STO covered by a film of $SrRuO_3$ (SRO), and STO covered by films of LAO,

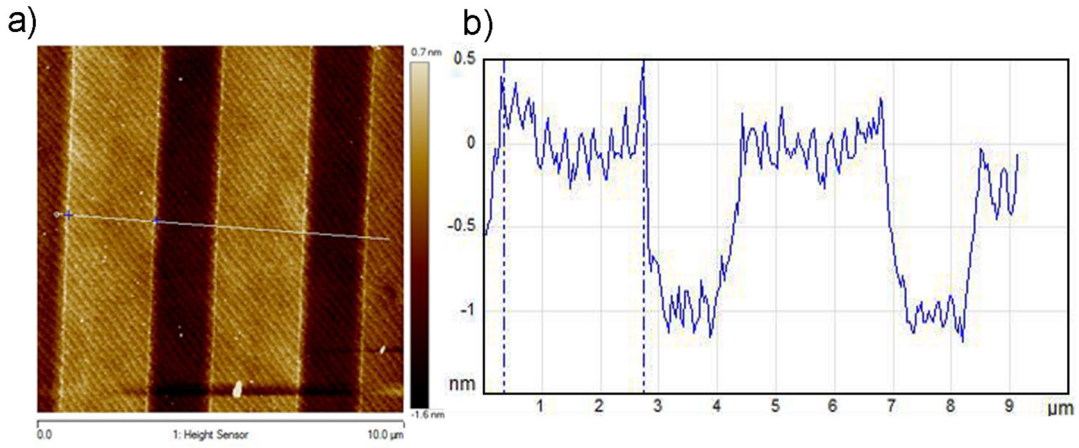

Figure 5.4 a) AFM image of LAO/STO sample, patterned with conducting stripes (brighter) spaced by insulating areas (darker). b) Section profile height of the patterned stripes along the white line in a). The conductive stripes are 2.4 μm wide, the spacing is 1.6 μm, and the vertical step on the LAO surface is just 1 *nm* high.

both irradiated (insulating interface) and non-irradiated (metallic q2DEG interface). Both in SRO/STO and in metallic LAO/STO, an appreciable hardening of the lowest-energy transverse mode in the STO was observed, but in the case of the q2DEG the effect is weaker than under a conventional metal film and its detection required a more refined experimental procedure, based on the use of a THz polarized field (parallel or orthogonal to the patterned stripes). This is interpreted as indirect evidence of plasmon polaritons in the q2DEG of LAO/STO, which can hardly be observed directly due to the strong absorption of the infrared-active modes in the strontium titanate (this is discussed at length in paper VI).

6 Nanostructure Characterization

In this chapter we will describe the electrical characterization of several structures that were patterned in the LAO/STO q2DEG using the low energy ion beam irradiation technique described in previous chapters. We will briefly describe the experimental setups utilized for the electrical measurements we performed. Then we report the most important results we obtained.

6.1 Experimental setup

For all electrical measurements the structures were contacted with pads prepared by optical lithography and DC magnetron sputtering of 20 *nm* titanium and 120 *nm* gold, followed by standard lift-off process. The contacts were connected to measurement sample holders with Au or AlSi bonding wires. All the electrical measurements from room temperature down to 2 *K* were performed in a physical properties measurement system (PPMS, Quantum Design). This system gives the possibility to scan the temperature down to 2 *K* and to apply magnetic field up to 14 T. The low temperature measurements (down to 20 *mK*) were performed in a helium dilution cryostat (Oxford Triton 200). The sample was mounted in a metallic Cu box to provide electromagnetic shielding from the environmental noise. A combination of a superconducting lead and mu-metal shields granted a protection from the dc magnetic field component, with a residual field of less than 100 *nT*. In order to suppress the effect of noise, twisted pair of superconducting NbTi/Cu lines were used, in combination with 2 stages of cryogenic filters. Specifically, a stage of Cu powder filters were installed at the cold stage of the refrigerator, low-pass RC filters with a cut-off frequency of 0.2 MHz at the 4 *K* stage and conventional EMI filters at room temperature. The sample box was equipped with a Helmholtz NbTi/Cu superconducting coil, capable of a maximum magnetic field of 10 *mT* orthogonal to the sample plane, and with a microwave antenna placed at 1 *mm* above the sample.

Electrical measurements on nanostructures were complemented by surface potential imaging, acquired using intermodulation electrostatic force microscopy (ImEFM, Intermodulation Products) [59]. ImEFM is an alternative to Kelvin Probe Force Microscopy; it uses resonance to enhance the force sensitivity of the cantilever (MikroMasch HQ:NSC15/Pt), allowing for much improved signal-to-noise ratio in a given measurement bandwidth (inverse of the signal integration time at each pixel).

The single-pass method works without voltage feedback to create an image of the contact potential difference between the Pt tip and sample, $V_{CPD} = \Phi_{surface} - \Phi_{tip}$. The AFM tip works very close to the surface (≈ 60 *nm*) resulting in high spatial resolution (nanometer size).

6.2 Retention of conductivity in SCO capped nanostructures

The measurements of electrical resistance of the bridges patterned in the LAO/STO q2DEG showed an unexpected increase of the sheet resistance in nanostructures (see Fig. 6.1). The sheet resistance is approximately constant for structures with 1 µm or wider width; below 1 µm an increase of the sheet resistance value is observed.

It is important to emphasize that this increase of the resistance is not due to edge effects during lithography process or ion beam irradiation. The sheet resistance was calculated using dimensions obtained from AFM images, thus lithographic error can be excluded. Irradiation itself may cause some deviation in size structure. SRIM calculations, discussed in Chapter 4, show that maximum side effect is about 4 *nm*, which corresponds to the film thickness and is then physically reasonable. Moreover, conducting structures with 50 *nm* linewidth were reproducibly measured, indicating that the maximum size of the side effect is 25 *nm*. Edge effects would not be enough to justify the increase in sheet resistance measured already in 1 µm structure where this would represent only a 2.5% reduction of the lateral width. One possible explanation to this increase of sheet resistance in nanostructures can be related to the non-homogeneity of the q2DEG that we discussed and that has already been reported in several works.

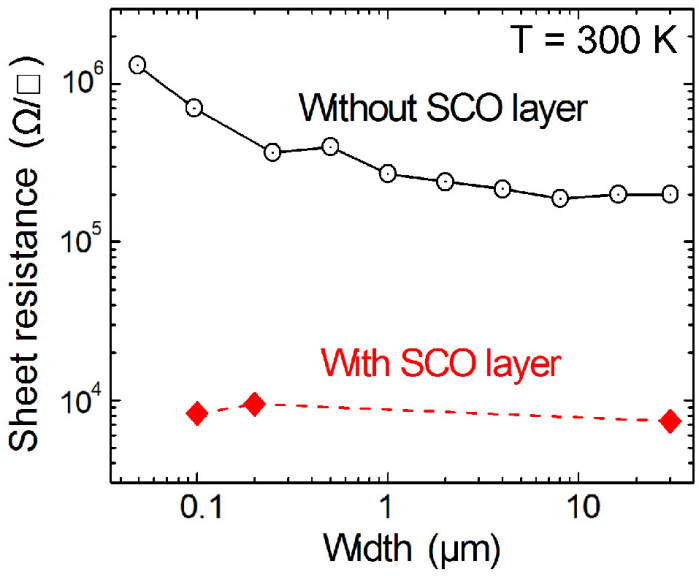

Figure 6.1 Sheet resistance as a function of patterned structure width for the LAO/STO sample without $SrCuO_2$ capping layer (empty circles) and for the LAO/STO sample with $SrCuO_2$ capping layer (full diamonds).

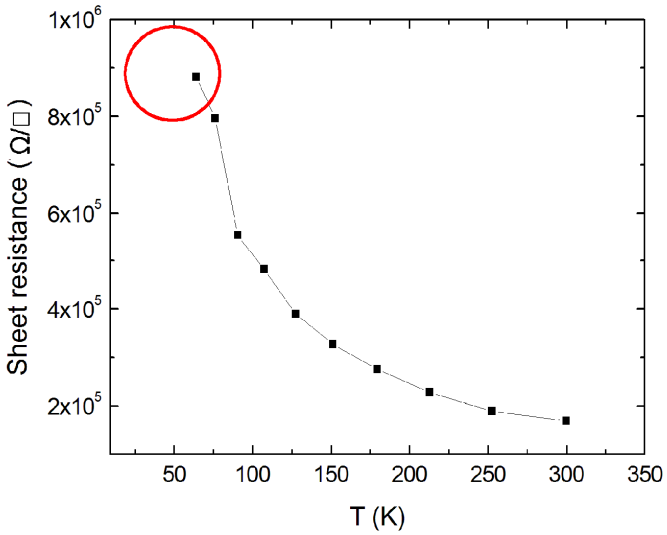

Figure 6.2 Sheet resistance for one of the nanostructured LAO/STO samples, increasing above measurement limit when the sample measured at low temperature (red circle shows last measurement point obtained before freeze-out).

The increase of the sheet resistance in nanostructures also created a practical problem: many nanostructures showed insulating behavior at low temperature, corresponding to a decrease in carrier concentration (so-called carrier freeze-out effect, see Fig. 6.2). In semiconductors, this effect is usually caused by trapping of mobile charge carriers on defects. This made the measurements on LAO/STO nano-patterned samples very complicated. For this reason we decided to fabricate new nanostructures in LAO/STO capped by an SCO layer that, as described in Chapter 2, is expected to significantly improve the properties of the LAO/STO interfacial q2DEG. We found that not only does the SCO capping layer improve the electrical conductivity of the LAO/STO samples on a macroscopic scale, but it also changes the electrical properties of the interface on nanoscale. Figure 6.1 shows that sheet

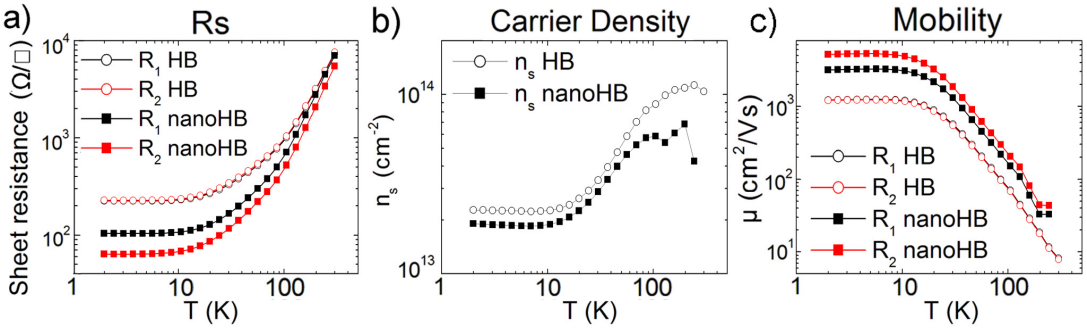

Figure 6.3 Electrical transport properties of macro- (HB) and nano-Hall bars (nanoHB) patterned in SCO-capped LAO/STO interface. Temperature dependence of a) sheet resistance, b) carrier density and c) mobility, for nanostructures (full squares) and macroscopic structures (empty circles). Sheet resistance and mobility represent data for two different segments of the same Hall bar (black and red). Both structures were fabricated on the same sample.

resistance of the SCO-capped structures is reduced by a factor of 10 as compared to non-capped ones, in agreement with results in [30]. It is also clear that the sheet resistance in the capped nanostructures is comparable to that measured in wider structures. We note that, while room temperature sheet resistance is increased in non-capped nanostructures, they never become insulating. We may interpret this lack of completely insulating behavior as a presence of two different non-homogenously distributed regions in the q2DEG, with high and low electrical conductivity, which is in line with a recent model of two types of carriers with low and high effective masses [60]. The two-region interpretation is further supported by the carrier freeze-out observed at low temperature in small structures. The size of lateral non-homogeneity was estimated from scaling arguments to be around 100 *nm* [38], in good agreement with our results.

Temperature dependences of sheet resistance, carrier concentration and Hall mobility of nano- and macroscopic Hall bars of the capped LAO/STO interface are presented in Fig. 6.3. The electrical transport properties are very similar in both structures irrespective of scale. We measured several different structures and all showed similar behavior. However, it appears that the carrier concentration in our samples shows stronger temperature dependence than that of [30], where carrier concentration was almost independent of temperature for a sample prepared under similar conditions to ours. While we have followed exactly the same recipe for sample fabrication as in [30], a minor variation in oxygen pressure or laser energy density during film growth may result in residual oxygen vacancies or other defects, *e.g.* Sr-La and Ti/Al intermixing, explaining the temperature dependence of carrier concentration in our samples.

6.3 Intermodulation electrostatic force microscopy

Considering the effect of the SCO capping layer on electrical properties, one can presume that it is affecting the non-homogeneity of the q2DEG, creating a more homogeneous conductive layer and avoiding the problem of high resistance for small structures.

For this reason we complemented our electrical measurements with intermodulation electrostatic force microscopy (ImEFM) imaging of the measured structures. ImEFM images of nanoring structures with linewidth of 300 *nm* are presented in Figs. 6.4(a-b). In both non-capped 4(a) and capped 4(b) structures one can clearly resolve the conducting ring from insulating surrounding, however the contrast, or change in contact potential difference, is much larger in the non-capped structure (as can be seen from the distance between the peaks in the histograms of Fig. 6.4 (c)). Figure 6.4(c) shows histograms of the images 6.4(a) and 6.4(b), where one can see that the non-capped structure has both lower V_{CPD} over the insulating region, and higher V_{CPD} over the conducting regions. Assuming that the Pt tip had fixed work function, we can conclude that capping results in both increase of the work function in the insulating region, and decrease in the conducting region. We also note that the non-capped structure shows a distinct difference in V_{CPD} between the

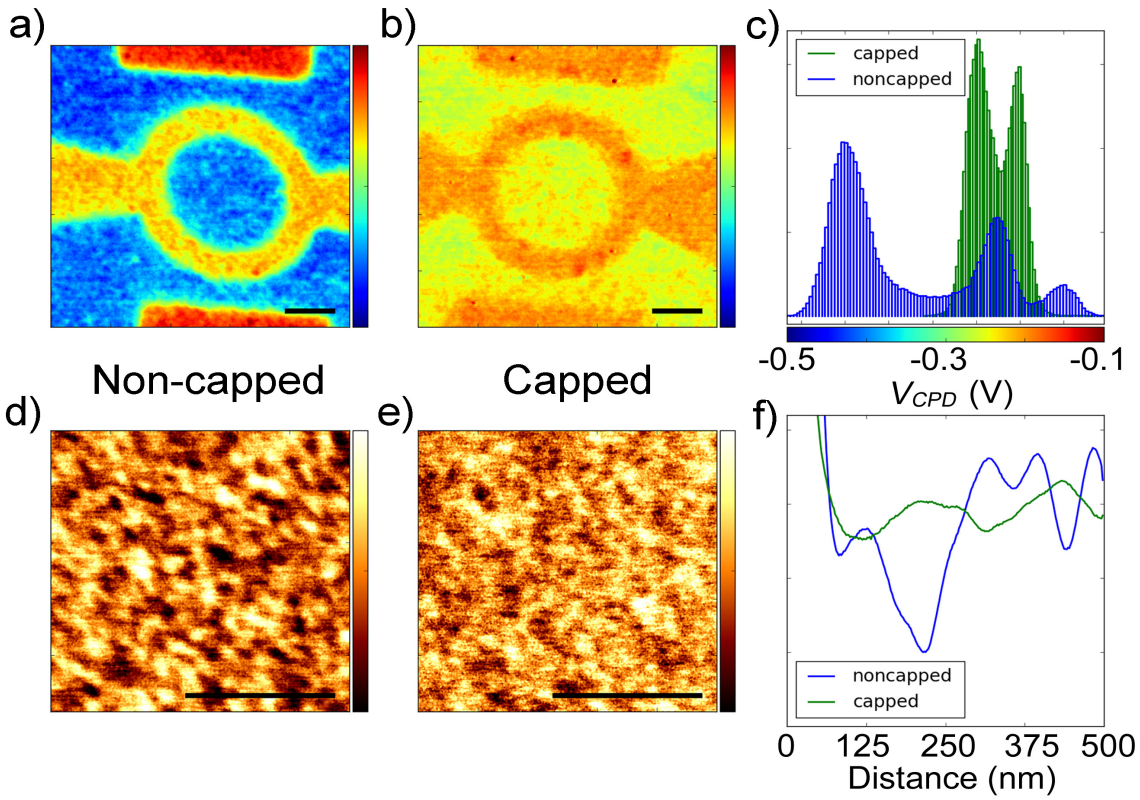

Figure 6.4 ImEFM images of the contact potential difference V_{CPD} of both non-capped (a and d) and capped (b and e) structures. The space bar in all images is 500 *nm*. Image histograms (c) show much higher contrast in the non-capped structure. Higher resolution scans (d and e) of the conducting lead region of each structure revealed non-omogeneity of V_{CPD}, where the radial auto correlation function (f) indicates a characteristic size of the variations in the range 130 *nm* in the non-capped sample. In a) and b) the color scale ranges between -0.5 and -0.1 V, in d) it ranges between -0.25 and -0.19 V, and in e) it ranges between -0.20 and -0.16 V.

conducing leads (ring), and the conducting gate electrodes. This difference may be due to the fact that the leads of the device were grounded during the measurement, whereas the gate was left floating.

The images 6.4(d) and 6.4(e) show higher resolution scans over the conducting lead region of both non-capped and capped samples respectively. One can clearly see granularity of V_{CPD} which we analyze by calculating the radial auto correlation function (ACF), plotted in Fig. 6.4(f). The rapid decay of the ACF at low distance is due to noise, whereas the first peak at larger distance gives the correlation length for variation in V_{CPD}, or the characteristic size of the 'puddles'. The capped sample has a smoother ACF, indicating a more homogeneous material. In contrast, the non-capped sample shows larger variation of the ACF at length scale around 130 *nm*.

ImEFM imaging provides more insights into the non-homogeneous nature of the q2DEG. Clear contrast in surface potential between insulating and conductive parts of nanostructures in ImEFM images proves that the electrical transport is indeed confined within patterned structures. It also rules out the possibility that fabrication errors can be a cause of spread in electrical transport properties in non-capped nanostructures (Figs. 6.4(a) and 6.4(b)). The non-homogeneous contrast is observed

in both capped and non-capped interfaces with a correlation length that agrees well with the estimations of the size of puddles we discussed earlier. ImEFM technique images variation in the work function of the interfacial layer, reflecting local changes in the Fermi energy, E_F. Within the free electron model with diffusive transport, variation in E_F reflects a change in charge concentration, and thereby conductivity. Therefore, the contrast in surface potential can be interpreted as due to the presence of islands with different resistivity in the conductive interface. This is further supported by the fact that similar contrast appears in two types of samples with different surface layers (LAO film in non-capped samples and STO film in capped ones). It is interesting to notice that there is a difference in non-homogeneity between the uncapped and SCO-capped samples, but it is smaller than one first would expect taking into account the difference in electrical transport properties. The exact microscopic nature of these non-homogeneities is not known; it can be due to variation of the LAO film stoichiometry [32], oxygen vacancies that tend to form clusters [33] or lateral variation of the dielectric constants in the LAO film or STO substrate. Being able to quantify the change in carrier density from the measured change in Fermi energy would strengthen our findings, but this requires additional modeling and measurements that are beyond this PhD work. Even if we assumed a free electron model description for the Fermi energy we would get:

$$dE/E = 2/3 \times dN/N \tag{6.1}$$

where E is the Fermi energy and N is the electron density. With ImEFM we measure the change dE, and we can say qualitatively that there is a corresponding change in carrier density dN. To quantify dN, we would need to independently measure (or model) the starting conditions E and N. Moreover, ImEFM does not measure directly E of the sample, but the difference E_{sample} - E_{tip}. When we compare two scans (or two regions within one scan, or different puddles) we get:

$$(E_1 - E_{tip}) - (E_2 - E_{tip}) = E_1 - E_2 = dE \tag{6.2}$$

At the same time it would not help to calibrate the work function of the AFM tip E_{tip}, in that case we would get an "absolute" measure of the Fermi energy relative to the vacuum level, while in equation (6.1) E is measured relative to the bottom of the conduction band.

6.4 Superconductivity in SCO capped nanostructures

SCO-capped structures showed superconducting transitions below 300 *mK*. A set of current-voltage characteristics for a ring with linewidth of 100 *nm* is shown in Fig. 6.5(a). From critical current dependence on temperature shown in Fig. 6.5(b), the critical temperature can be estimated (extrapolating Ic to zero) to about 280 *mK* for a ring and 200 *mK* for a wire of the same width (100 *nm*), which is comparable to the

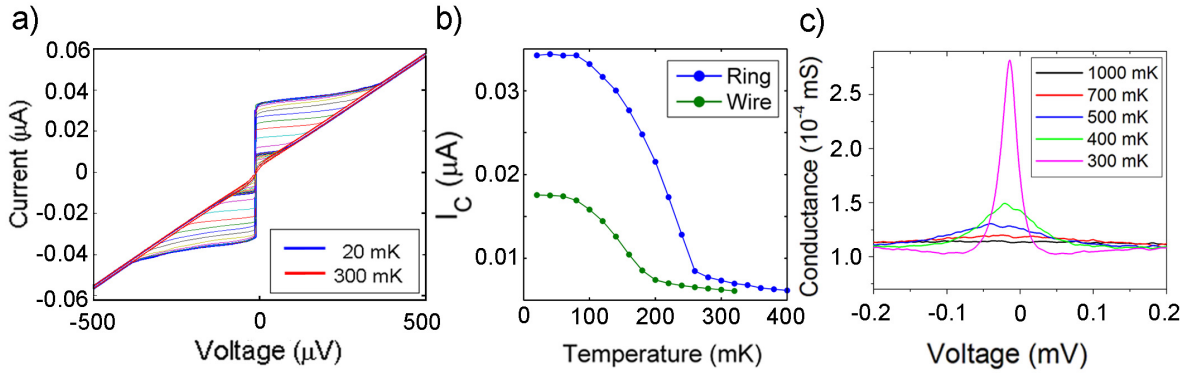

Figure 6.5 Superconducting properties of SCO-capped nanostructures: a) current-voltage characteristics of a 100 *nm* ring as function of temperature (in 20 *mK* steps), b) Critical current versus temperature for a ring and a wire with the same width (100 *nm*), and c) Conductance versus voltage above critical temperature.

≈200 *mK* for non-capped structures. Furthermore, the conductance as a function of the voltage (Fig. 6.5(c)) shows the persistence of a non-linear behavior above the superconductive transition, resulting in the long "tails" in the estimation of the critical current (see Fig. 6.5(b)). This is in contrast to the previously reported absence of superconductivity down to 60 *mK* in SCO capped interfaces [61]. Superconductivity in the LAO/STO interface is believed to originate from the STO substrate [62] [8]. The critical temperature of doped STO follows a dome-like behavior as a function of bulk carrier concentration [63]. Therefore, different behavior can be explained as different doping in the LAO/STO interface. Sheet carrier concentration in our samples (2×10^{13} cm^{-2}) is about 2 times higher than that (1×10^{13} cm^{-2}) reported in [30]. Assuming a reasonable estimation of thickness of the superconducting layer of about 10 *nm* [31], a corresponding bulk carrier concentration in our samples is about 2×10^{19} cm^{-3}. Optimal carrier concentration in STO is about 10^{20} cm^{-3} corresponding to a

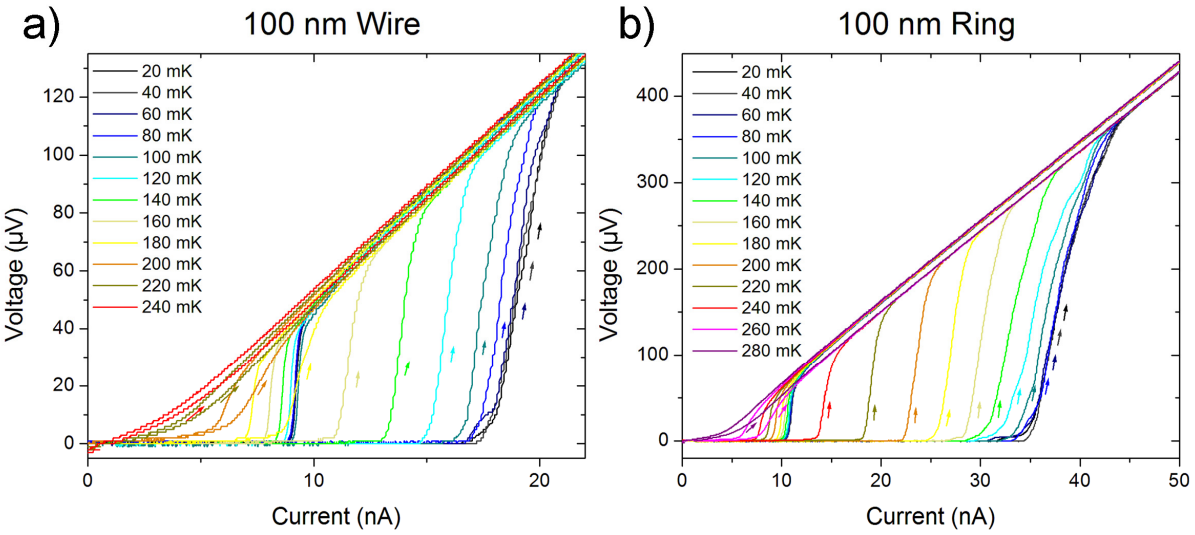

Fig. 6.6. Details of the IVC of a) a wire and b) a ring, with 100 *nm* linewidths. Data show the IVCs hysteretic behaviour as a function of the temperature.

maximum critical temperature of about 0.3 *K* [63] [64]. This means that our samples are under-doped, and a small deviation of carrier concentration may bring the system into the non-superconducting regime. Moreover, comparison between different interfaces is complicated by uncertainty in the thickness of the conducting layer.

The superconducting transition appears across 0.2-0.3 *K* in our samples but the I-V characteristics show non-linear behavior even above the "bulk" critical temperature (see Fig. 6.5(b)). The non-linear shape of the I-V characteristics is reminiscent of a network of resistively-shunted Josephson junctions. Remnants of this non-linearity are observed at temperature up to 700 *mK* which may be interpreted as indicating superconductivity at higher temperatures. Two-gap superconductivity has been theoretically predicted [65] and experimentally observed [66] [67] in STO. While there is no general agreement on interpretation, these data may indicate presence of percolative superconducting transition in the LAO/STO interface, related to a presence of two types of carriers with low and high effective mass [67]. An alternative interpretation is suggested in [66] as due to pre-formation of Cooper pairs above the critical temperature.

Details of the IVCs of the nanoring and nanowire with linewidth of 100 *nm*, measured at different temperatures, are shown in the Fig. 6.6. Each IVC is a result of 50 averages. All IVCs show sharp switching from superconducting to normal state at critical current, I_C, when bias current is swept from zero to the maximum. In normal state, all IVCs show linear behavior even at very high bias currents. When bias current is swept back to zero, switching to resistive state occurs at significantly lower current (retrapping current, I_R) resulting in hysteretic behavior. The hysteresis appears in all IVCs just below the critical temperature. The hysteresis is quantified by the ratio I_R/I_C (see Table I) and shows a clear dependence on the structure size; furthermore, the hysteretic behavior is more pronounced in the rings, were the current density J_C is higher than in the rings. The temperature dependence of the critical current I_C, and re-trapping current I_R, are reported in Fig. 6.7. The normal resistance of the structures is temperature independent and reported in Table I.

Table I

Structure	T_C (*mK*)	I_C, *20 mK* (*nA*)	J_C, *20 mK* (kA/cm^2)	I_R/I_C, *20 mK*	R_N (Ω)	I_CR_N, *20 mK* (μV)
R100	280	34	1.7	0.25	$9.2x10^3$	312
R200	250	210	5.3	0.11	$5.2x10^4$	1100
R300	280	235	3.9	0.07	$7.3x10^3$	1700
W100	230	18	1.8	0.45	$7.0x10^3$	122
W200		30	1.5	0.33	$4.6 x10^3$	138

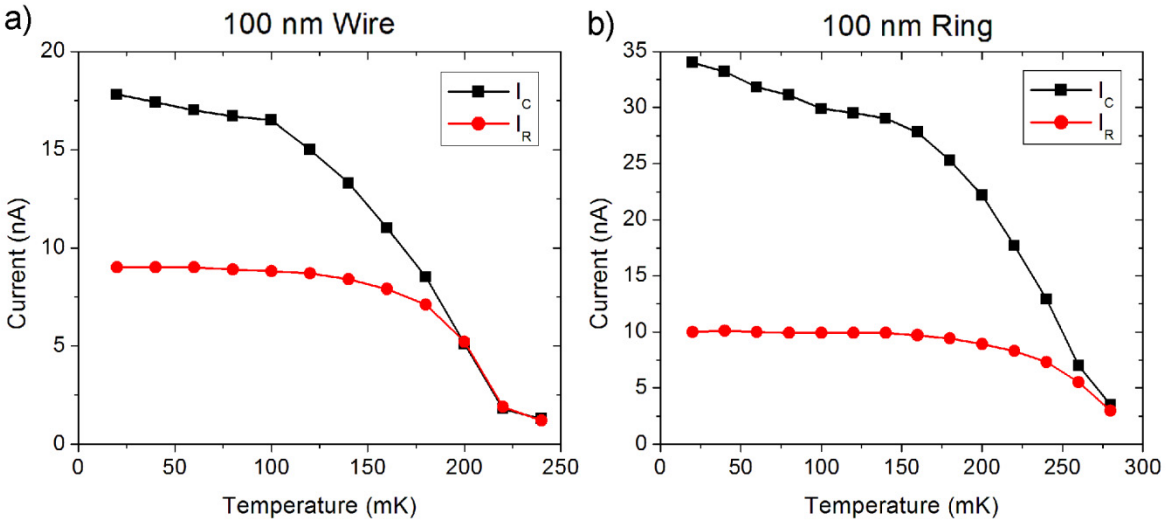

Fig. 6.7 I_R and I_C dependence on temperature for a wire and a ring with 100 *nm* linewidth.

6.5 SQUID-like behavior in LAO/STO nanorings

We performed measurements of critical current dependence on applied external magnetic field in nanostructures fabricated at the SCO capped LAO/STO interface.

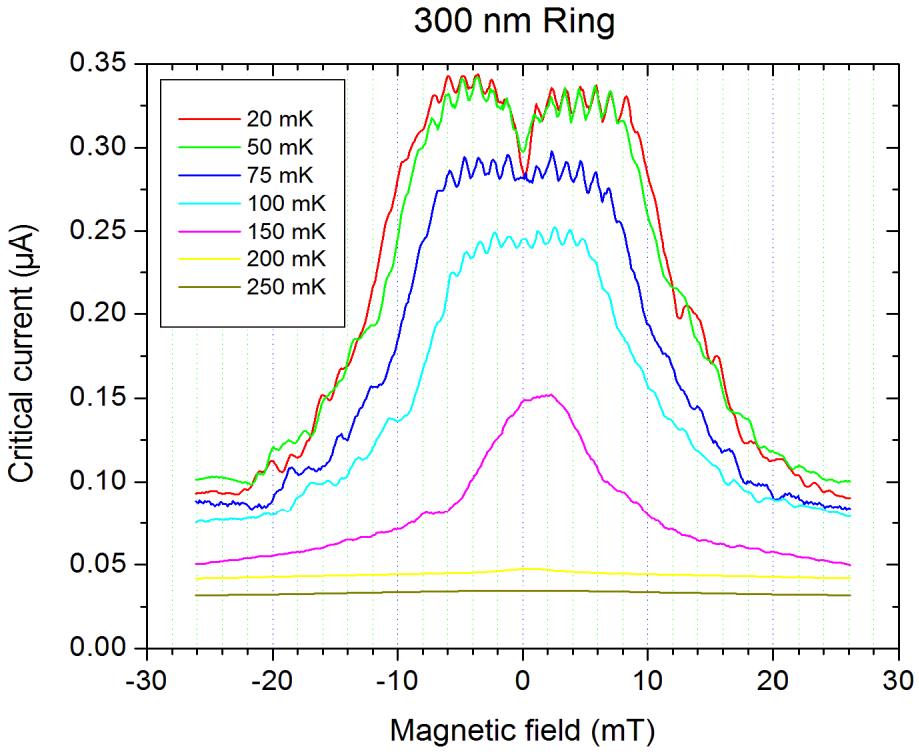

Figure 6.8 Critical current versus the external applied magnetic field for 300 *nm* linewidth nanoring. The dependence is shown for temperature ranging from critical temperature (250 *mK*) down to base temperature (20 *mK*).

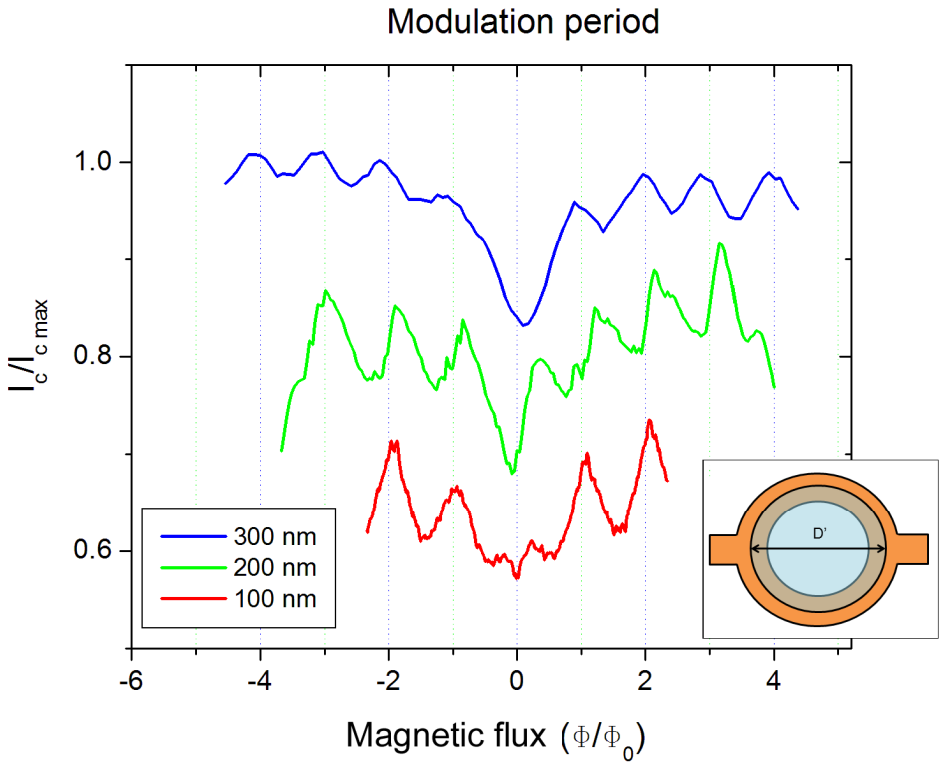

Figure 6.9 Critical current versus the normalized magnetic flux in the loop for rings with different linewidth (300, 200 and 100 *nm*). The data overlap, but for the sake of clarity the green and the red curves are shifted down of 0.2 and 0.4 respectively. The inset shows the effective area assumed for the normalization of the curves reported were *D'* represents the effective diameter.

Averaged critical current was measured as a function of the magnetic field, for nanorings with linewidth of 300, 200 and 100 *nm*. Measurements at different temperatures below the T_C for the 300 *nm* ring are shown in Fig. 6.8. A bell-shape type dependence of the critical current versus magnetic field appears just below the T_C. A periodic modulation can be seen only at temperature below 100 *mK* (about half of the critical temperature). The bell-shape is seen at all temperatures but becomes broader with decreasing temperature. The critical current has maximum at zero magnetic field at high temperatures above 100 *mK*. However, a clear minimum in the critical current at zero magnetic field appears below 75 *mK*.

Observation of critical current modulation under applied perpendicular magnetic field is an unambiguous evidence of the long-range superconducting coherence in our nanorings. A similar behavior is observed in all the nanorings with an oscillation period of the critical current that scales with the area of the ring. Fig. 6.9 shows critical current modulation for rings with linewidth of 100, 200 and 300 *nm* (corresponding to inner diameters of 400, 800 and 1200 *nm*) as a function of magnetic flux in the ring. The period corresponds to exactly one single flux quantum $\Phi_0 = h/2e$, assuming an effective area of the ring calculated as $A_{eff} = \pi R_{eff}^2$, where $R_{eff} = R + w/2$, [68] as illustrated in the inset to Fig. 6.9.

From the amplitude of oscillations, one can estimate the screening parameter $\beta_L = 2I_C L/\Phi_0$, and ring inductance L. This gives estimates of the SQUID inductance about 50 nH for 200 and 300 *nm* rings. This is about 5 orders of magnitude higher than geometric inductance calculated from the geometrical size of the rings, $L \approx \mu_0 D$. Such large inductance arises from the kinetic inductance of the superconductor, $L_K = \mu_0 \Lambda/2$, where $\Lambda = \lambda_L^2/d$ is the Pearl length of the thin film, λ_L is the London penetration depth, and *d* is the thickness of the conduction layer.

The origin of the observed SQUID-like modualtion is still not totally clear. The superconducting constrictions with dimensions much less than the coherence length of the superconductor, ξ can show "true" Josephson junction behavior with current-phase relation close to sinusoidal [69]. The superconducting nanowires have been extensively studied in low-temperature superconductors. It has been shown that dynamic behavior of clean short superconducting nanowires is largely determined by fluctuation effects and formation of phase slip centers (PSC) [70]. The order parameter in the PSC becomes zero in close similarity to weak links and Josephson junctions. According to previous estimations, the coherence length ξ of the LAO/STO is about 100 *nm* [31]; the width of our nanowires is about the same as the coherence length, but their length greatly exceeds ξ. Even such structures can show Josephson-like effects, such as Shapiro steps under external microwave radiation [71]. In this case, the electrical transport in clean structures is determined by diffusive motion of Andreev vortices resulting in characteristic "flux-flow" IVCs with non-linear normal resistance that increases with increasing bias current [72]. Such behavior has been observed in nanowires made from high-temperature superconductors with very small coherence length. Our nanowires, despite their dimensions greatly exceed the coherence length, show IVCs with linear normal resistance.

This may be caused by a presence of non-homogeneous distribution of supercurrent within the nanowire and formation of constrictions with much smaller dimensions and PSC formation. Another possibility is presence of weak-links in grain boundaries or normal metal regions in the LAO/STO that have been experimentally observed and theoretically described. The critical current density of our nanowires is in the range of ~1kA/cm^2 (assuming a thickness of the superconducting layer of about 10 *nm*), which is close to the Ginzburg-Landau maximum critical current density.

6.6 Switching current distribution measurements

The current-voltage characteristics of all the structures showed a large variation in the critical current I_C. A detail of repeated current-voltage characteristics measured at 20 *mK* of the ring with 300 *nm* linewidth is reported in Fig. 6.10 (a). To understand the dynamics of the critical current variations and better estimate a median critical current, we measured switching current distributions (SCD) as a function of the temperature and magnetic field for all the structures. The measurement of the SCDs was performed using a conventional time of flight (TOF) electronics [73]. The current bias was ramped at a rate of 60 μA/s leading to a decay of the junction from the dissipation-less to the resistive state [74] [75]. After the escape, the current is ramped

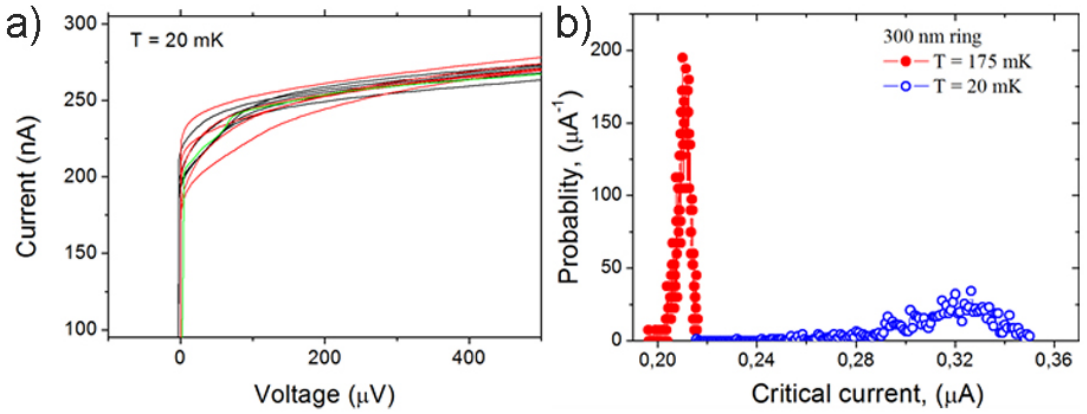

Fig. 6.10 (a) Current-voltage characteristics of a 300 *nm* linewidth ring measured at 20 *mK* showing large spread of critical current. (b) Switching current distribution of the same ring measured at 20 *mK* and 150 *mK*. There is a large increase in the width of the histogram at low temperature.

down to zero in 20 *ms* to cool down the device from the heat locally created in the resistive state. Examples of histograms corresponding to a 300 *nm* ring measured at 20 *mK* and 175 *mK* are shown in Fig. 6.10 (b). Against what usually expected, the width of the switching distribution significantly increases with decreasing temperature, explaining the observed spread of critical current in Fig. 6.10 (a). This temperature dependence can be explained by non-equilibrium Josephson dynamics in weakly underdamped Josephson junctions [76]. A similar dependence of distribution width was observed in high-Tc superconducting stacks of intrinsic Josephson junctions [77]. It was explained as a cross-over from 3D to 2D case with lowering of the temperature. This could be possible in our case also, assuming that the nanowires are arrays of S-N-S junctions.

The magnetic field dependence of SCD for a 300 *nm* linewidth ring at 20 *mK* is reported in Fig. 6.11 together with estimated mean current I_{mean} (left inset) and sigma variation (right inset). The SCD shows a more detailed picture of the I_C dependence on the magnetic field. The minimum in zero magnetic field corresponds to a spread in the sigma distribution that becomes narrower for magnetic fields above $\approx 1\ mT$. The sigma then oscillates with a periodic dependence on the magnetic field (see right inset in Fig. 6.11).

At the same time, two modulation of the I_C can be observed, shifted by 1.3 *mT*, that corresponds to a single flux quantum. This bi-stable magnetic field dependence of critical current distribution can be explained can be explained by the high inductance value, as explained in previous paragraph. At high screening parameters values, β_L, flux in the SQUID loop is not a single-value of an applied external magnetic flux and therefore shows metastable behavior [78]. Furthermore, the periodic modulation is not centered on the minimum in zero magnetic field, as can be deduced by the asymmetric relative maximum at about $\approx 0.5\ mT$. The SCD distribution is then a slightly asymmetric convolution of the periodic modulation and the dip in zero magnetic field. One may assume that knowing the exact shape of the dip we would be able to deconvolute the function and obtain a uniform periodic modulation.

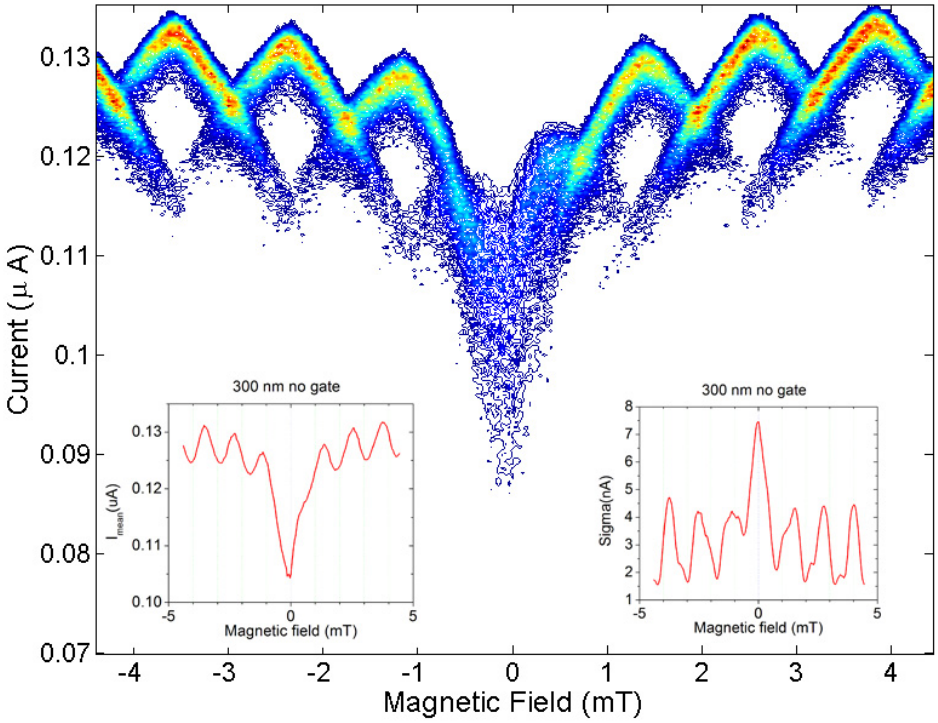

Fig. 6.11. Switching current distribution for a ring with 300 *nm* linewidth, as a function of magnetic field, measured at 20 *mK*. The inset on the left shows the mean current I_{mean}, and the inset on the right shows the critical current sigma as a function of the magnetic field. The appearance of two current distributions, shifted by a flux quantum, indicates a bi-stable nature.

The mean critical current I_{mean} obtained from the SCD measurements are reported as a function of the temperature, for three different ring structures, in Fig. 6.12. For all structures, mean critical current is suppressed at low temperature corresponding to the observation of local minimum for I_C at zero magnetic field shown in Fig. 6.8 and Fig. 6.9.

The observation of a minimum in critical current at zero magnetic fields, at low temperature for all nanostructures (rings and wires), is a remarkable feature. There are several possible physical explanations to the appearance of such dip in the critical current. The first one is that the dip can be explained by a proximity effect with ferromagnetic domains that co-exist with superconductivity in the LAO/STO [9] [79]. The presence of ferromagnetic patches can lead to formation of the S-F-S Josephson junctions within a nanowire. Such junctions can show reentrant Josephson critical current in S-F-S structures with intrinsic π-shift [80]. The Josephson coupling in S-F-S structures changes as a function of temperature from 0 to π due to temperature dependent decay of the superconducting wave function in the ferromagnet. When odd number of junctions with intrinsic π-shift is included in the superconducting ring, it results in the minimum of critical current at the zero magnetic field. The reentrance of supercurrent requires very specific conditions to be fulfilled and assuming random

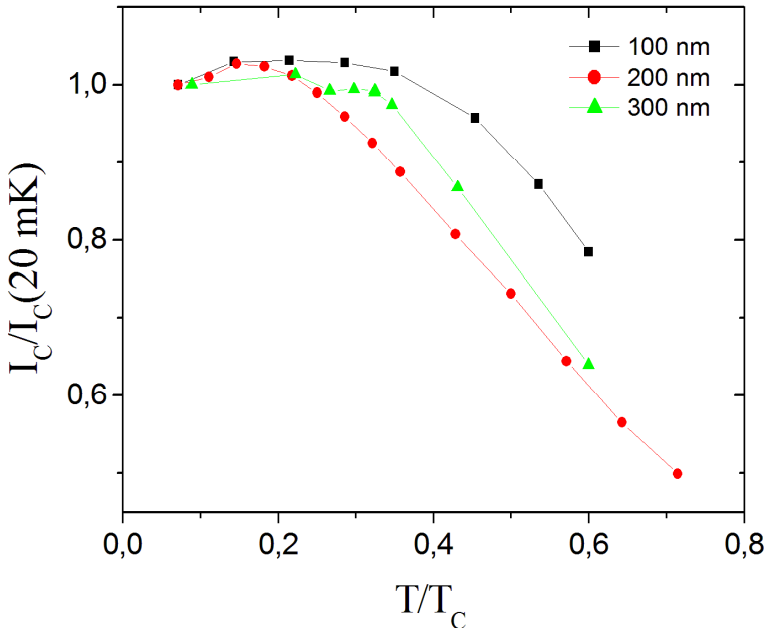

Fig. 6.12. Mean critical current vs. temperature obtained from the switching current distributions for the rings with 300, 200 and 100 *nm* linewidth. The temperature has been normalized to the superconducting transition temperature, and the critical current to the value at the lowest temperature (20 *mK*). The maximum in critical current seems to occur at a temperature somewhat larger than the lowest one.

nature of ferromagnetic domains, it is hard to expect similar behavior for different nanorings.

Another possibility is an induced spin-triplet superconducting correlations in the ferromagnetic domains [81] [82]. It has been theoretically predicted that Josephson current through half-metallic ferromagnet would have temperature dependence qualitatively in agreement with our results presented in the Fig. 6.12. However these scenarios cannot be confirmed (or rejected) completely only by the results of our experiments. Finding a clear explanation to all the results we present here will require further experiments that are beyond the aim of this PhD project.

7 Conclusions

In this final chapter we will discuss the limits and drawbacks of our work, and possible future experiments to continue and complete our study. In the end we will summarize all the results achieved in this work.

7.1 Critical discussion

In the previous sections we discussed in detail all the experiments that were performed, and we stressed all the results and information achieved. However to fully appreciate the extent of our work, it is also important to discuss what are its limits, what problems remain to be solved, and what are our plans to address these issues.

First of all the low energy Ar^+ irradiation technique we presented gives very reproducible and durable results for the patterning of thin LAO layers. However, as we discussed, there is a strong dependence of the time of irradiation required to induce the MIT transition from the thickness of the LAO film. We reported data for samples up to 15 u.c. thick, but from our experiments we noticed that for thicker samples (20 u.c. and over) the irradiation time required is so long that the ions start to produce oxygen vacancies in the STO substrate and the interface never reaches the complete insulating state even if the resistance is increased (same thing that happen in the case of high energy irradiation, see Chapter 4). For this reason our technique cannot be used, with the described parameters, to pattern LAO/STO sample with thick LAO layers (*i.e.* $\geq$ 20 u.c.). Further studies are required to establish if it is possible to tune some parameters to make the technique effective in case of thick LAO films and what condition would be required to achieve such result.

The resolution of our patterning technique, as we discussed, is currently limited only by the resolution of the E-beam lithography, and can thus be improved well below the 50 *nm* reported in this work. We have already performed experiments to optimize our E-beam process (exposure times, proximity corrections, resist used etc.), and we aim to reduce the resolution to $\approx$ 25 *nm*. However we can expect a physical limit to the resolution, related to the edge under-irradiation effect that we described in Chapter 6. There is indeed a minimum size below which the edge effect will be corresponding to the total dimension of the structure, effectively shunting the conductivity. From the theoretical considerations we presented in our work we can speculate this side effect is in the order of few nanometers, however it would be

interesting to obtain smaller and smaller structures with the E-beam lithography, in order to experimentally find this value and verify if it corresponds to our hypothesis.

We discussed the effects of the Ar ion irradiation on the LAO/STO interface and we found evidence that clearly relate the induced MIT to the Ar implantation. We proposed a scenario where Ar implantation is creating defects in the LAO/STO that are acting as traps for electrons destroying the conductivity. However, the exact nature of these defect states is not known yet. Further investigations of the defects created by Ar irradiation could give more information about the origin of the electron gas at the LAO/STO interface. These studies may include photoinduced transient current spectroscopy or deep-level transient spectroscopy experiments.

We discussed also the possibility of restoring the conductive state of the LAO/STO interface with a high temperature annealing. However we also reported that a small amount of material can still be removed by the irradiation, so the final state will not be exactly the same as after the deposition even if the electrical characterization shows identical results. For this reason we can ask ourselves if this process can be iterated, *i.e.* if it is possible to write, and then delete and rewrite new structure on the same sample with additional step of annealing and irradiation. Open questions are if the process of irradiation plus annealing would affect the effectiveness of a second attempt of patterning on the same sample, and how many times would be possible to repeat these steps before the sample is too deteriorated.

Our measurements of superconducting quantum interference in nanorings indicate influence of ferromagnetic impurities on superconducting order parameter in the LAO/STO. This supports the proposed model of electronic phase separation of the q2DEG at the LAO/STO interface into superconducting and normal metal magnetic domains. However, the distribution of these domains in our nanostructures is not known. It is of great interest to establish a correlation between electrical transport properties and the microscopic distribution of the domains by, e.g. low-temperature Kelvin probe AFM or STM. Further, a possible effect of strong spin-orbit coupling could be revealed by experiments involving measurements of superconducting properties under an applied magnetic field parallel to the interface plane. This may open new applications of the LAO/STO interface to realize and study topological superconducting states.

7.2 Results summary

In this work we presented a robust and reliable technique to pattern the q2DEG at the LAO/STO interface, we used it to pattern structure down to 50 *nm* and we investigated those structures' electrical transport properties.

First of all, we reported the possibility to induce a metal-insulator transition (MIT) at the LAO/STO interface using low energy Ar ions irradiation. We showed that low energy and short irradiation time are the keys to not induce the formation of oxygen vacancies in the STO substrate. In order to understand the cause of the transition, we presented a detailed study of the effect of low energy Ar irradiation on the electrical properties and on the microstructure of the LAO/STO system. Atomic

force microscope (AFM), scanning transmission electron microscope (STEM) and X-ray photo-emission spectroscopy (XPS) investigations demonstrated that the MIT is strongly related to the implantation of Ar during the irradiation. Furthermore, we showed that the induced MIT is reversible and initial conductive state can be fully restored through a high temperature post-annealing process.

We showed then how the low energy Ar ions irradiation can be used in conjunction with e-beam lithography to pattern working structures at the LAO/STO interface down to 50 *nm*.

We then described the results of electrical characterization of nanostructures patterned with our technique. We report that an $SrCuO_2$ capping layer can drastically improve nanostructures at the LAO/STO interface by granting retention of electrical transport properties comparable to the ones observed in large scale structures.

We report the observation of SQUID-like modulation in nanoring structures patterned at the SCO capped LAO/STO interface. This can be explained by the presence of non-homogeneous distribution of supercurrent within the structure with consequent formation of constrictions acting as phase slip centers, or by the presence of weak-links in grain boundaries or normal metal regions in the LAO/STO.

Finally we report the remarkable feature of a minimum in critical current at zero magnetic fields, at low temperature, for all nanostructures. This could be explained by a proximity effect with ferromagnetic domains that co-exist with superconductivity in the LAO/STO, or by induced spin-triplet superconducting correlations in the ferromagnetic domains.

Acknowledgements

First of all, I would like to thank Alexei Kalabukhov and Dag Winkler for giving me the possibility to work on this PhD project.

I am very grateful to Tord Claeson, for the support he gave me in the writing of this thesis and all the articles.

This work was supported by the Swedish Research Council, The Knut and Alice Wallenberg foundation, and Swedish Institute Visby program. The support from the Swedish Infrastructure for Micro- and Nanofabrication Myfab is appreciated.

Special thanks to Eric Andersson for all the work we did together and for the very interesting results we shared.

Many thanks go to Nikolina Tuzla and Eva Olsson that made an amazing work on my samples.

Thanks to David Haviland and Riccardo Borgani for the possibility to have such a fruitful collaboration.

Thanks to Fabio Miletto Granozio, Paolo Calvani and the entire group in Rome to give me the possibility to take part in their interesting experiment.

I want to thank Per Hyldgaard and Mikael Fogelström, for all the nice discussions we had together.

A special thanks to Niklas Lindvall that gave me a big editorial help, and to Luca Galletti for the amazing cover image.

I want to thank also the people that I met during this experience in the Quantum Device Physics group and that shared with me a piece of their life. Thanks to Minshu Xie, Maria Ekström, Tom Yager, Sumedh Mahashabde, Gunta Kunakova, Nicola Crovato, Sophie Charpentier, Reza Baghdadi, Marco Arzeo, Andrè Dankert, Astghik Adamyan, and all the others.

Thanks to the people that have been my colleagues in the FFF board, Beniamino Iandolo, Matteo Bazzanella, Anna Clemens, Yevgeniy Korniyenko, Hampus Linander, Manfred Kerner and all the others.

All my gratitude goes to my family, my mother Consiglia, my father Giulio, and my sister Silvia, they have always supported and believed in me during all my years of study.

Finally, thanks to the most important person in my life, my best friend, my travel companion, my inspiration, my lobster, my Princess Bubblegum, *Silvia*.

8 Bibliography

[1] H.-R. Wenk and A. Bulakh, Minerals: Their Constitution and Origin, New York, NY: Cambridge University Press, (2004).

[2] J. B. Goodenough, Localized to Itinerant Electronic Transition in Perovskite Oxides, Springer Berlin Heidelberg, (2001).

[3] D. B. Chrisey and G. K. Hubler, Pulsed Laser Deposition of Thin Films, John Wiley & Sons, (1994).

[4] A. Y. Cho and J. R. Arthur, "Molecular beam epitaxy", *Prog. Solid State Chem.,* **10**, 157, (1975).

[5] K. Choy, "Chemical vapour deposition of coatings", *Progress in Material Science,* **48**, 57, (2003).

[6] R. Behrisch, Sputtering by Particle bombardment, Berlin: Springer, (1981).

[7] A. Ohtomo and H. Hwang, "A High-Mobility Electron Gas at $LaAlO_3/SrTiO_3$ Heterointerface", *Nature,* **427**, 423, (2004).

[8] S. Gariglio, N. Reyner, A. D. Caviglia and J.-M. Triscone, "Superconductivity at the $LaAlO_3/SrTiO_3$ Interface", *J. Phys.: Condens. Matter,* **21**, 164213, (2009).

[9] J. A. Bert, B. Kalisky, C. Bell, M. Kim, Y. Hikita, H. Y. Hwang and K. A. Moler, "Direct Imaging of the Coexistence of Ferromagnetism and Superconductivity at the $LaAlO_3/SrTiO_3$ Interface", *Nature Physics,* **7**, 767, (2011).

[10] B. M. Shalom, Rakhmilevitch, Palevski and Dagan, "Tuning Spin-Orbit Coupling and Superconductivity at the $SrTiO_3/LaAlO_3$

Interface: A Magnetotransport Study", *Physical Review Letters,* **104**, 12, (2010).

[11] A. Tebano, E. Fabbri, D. Pergolesi, G. Balestrino and E. Traversa, "Room-Temperature Giant Persistent Photoconductivity in $SrTiO_3/LaAlO_3$ Heterostructures", *ACS Nano,* **6**, 1278, (2012).

[12] J. Mannhart and D. G. Schlom, "Oxide interfaces - an opportunity for electronics", *Science,* **327**, 1607, (2010).

[13] D. G. Schlom and J. Mannhart, "Oxide electronics: Interface takes charge over Si", *Nature Materials,* **10**, 168, (2011).

[14] A. D. Caviglia, S. Gariglio, C. Cancellieri, B. Sacèpè, A. Fète, N. Reyren, M. Gabay, A. F. Morpurgo and J.-M. Triscone, "Two-dimensional quantum oscillations of the conductance at $LaAlO_3/SrTiO_3$ interfaces", *Physical Review Letters,* **105**, 23, (2010).

[15] M. Basletic, J.-L. Maurice, C. Carrétéro, G. Herranz, O. Copie, M. Bibes, E. Jacquet, K. Bouzehouane, S. Fusil and A. Barthélémy, "Mapping the spatial distribution of charge carriers in $LaAlO_3/SrTiO_3$ heterostructures", *Nature Materials,* **7**, 621, (2008).

[16] G. Herranz, M. Basletić, M. Bibes, C. Carrétéro, E. Tafra, E. Jacquet, K. Bouzehouane, C. Deranlot, A. Hamzić, J.-M. Broto and e. al., "High Mobility in $LaAlO_3/SrTiO_3$ Heterostructures: Origin, Dimensionality, and Perspectives", *Phys. Rev. Lett.,* **98**, 216803, (2007).

[17] S. Thiel, G. Hammerl, A. Schmehl, C. W. Schneider and J. Mannhart, "Tunable Quasi–Two-Dimensional Electron Gases in Oxide Heterostructures", *Science,* **313**, 1942, (2006).

[18] H. W. Jang, D. A. Felker, C. W. Bark, Y. Wang, M. K. Niranjan, C. T. Nelson, Y. Zhang, D. Su, C. M. Folkman, S. H. Baek, S. Lee, K. Janicka, Y. Zhu, X. Q. Pan, D. D. Fong, E. Y. Tsymbal, M. S. Rzchowski and C. B. Eom, "Metallic and Insulating Oxide Interfaces Controlled by Electronic Correlations", *Science,* **331**, 886, (2011).

[19] G. Herranz, F. Sànchez, N. Dix, M. Scigaj and J. Fontcuberta, "High mobility conduction at (110) and (111) $LaAlO_3/SrTiO_3$ interfaces", *Scientific report,* **2**, 758, (2012).

[20] M. P. Warusawithana, A. A. Pawlicki, T. Heeg, D. G. Schlom, C. Richter, S. Paetel, J. Mannhart, M. Zheng, B. Mulcahy, J. N. Eckstein, W. Zander and J. Schubert, "$LaAlO_3$ stoichiometry is key to electron liquid formation at $LaAlO_3/SrTiO_3$ interfaces", *Bull. Am. Phys. Soc.,* **55**, (2010).

[21] A. Brinkman, M. Huijben, M. van Zalk, J. Huijben, U. Zeitler, J. C. Maan, W. G. van der Wiel, G. Rijnders, D. H. A. Blank and H. Hilgenkamp, "Magnetic effects at the interface between non-magnetic oxides", *Nature Materials,* **6**, 493, (2007).

[22] L. Li, C. Richter, J. Mannhart and R. Ashoori, "Coexistence of Magnetic Order and Two-Dimensional Superconductivity at $LaAlO_3/SrTiO_3$ Interfaces", *Nature Physics,* **7**, 762, (2011).

[23] N. Nakagawa, H. Y. Hwang and D. A. Muller, "Why Some Interfaces Cannot Be Sharp", *Nature Materials,* **5**, 204, (2006).

[24] W. Siemons, G. Koster, H. Yamamoto, W. Harrison, G. Lucovsky, T. Geballe, D. Blank and M. Beasley, " Origin of Charge Density at $LaAlO_3$ on $SrTiO_3$ Heterointerfaces: Possibility of Intrinsic Doping", *Phys. Rev. Lett.,* **98**, 196802, (2007).

[25] A. S. Kalabukhov, R. Gunnarsson, J. Boriesson, E. Olsson, T. Claeson and D. Winkler, "The role of oxygen vacancies in $SrTiO_3$ at the $LaAlO_3/SrTiO_3$ interface", *Phys. Rev. B,* **75**, 121404, (2007).

[26] Y. Chen, N. Pryds, J. E. Kleibeuker, G. Koster, J. Sun, E. Stamate, B. Shen, G. Rijnders and S. Linderoth, "Metallic and Insulating Interfaces of Amorphous $SrTiO_3$-Based Oxide Heterostructures", *Nano Letters,* **11**, 3774, (2011).

[27] P. R. Willmot, S. A. Pauli, R. Herger, C. M. Shleputz, D. Martoccia, B. D. Patterson, B. Delley, R. Clarke, D. Kumah, C. Cionca and Y. Yacoby, "Structural Basis for the Conducting Interface between $LaAlO_3$ and $SrTiO_3$", *Phys. Rev. Lett.,* **99**, 155502, (2007).

[28] L. Qiao, T. C. Droubay, V. Shutthanandan, Z. Zhu, P. V. Sushko and S. A. Chambers, "Thermodynamic instability at the stoichiometric $LaAlO_3/SrTiO_3(001)$ interface", *J. Phys.: Condens. Matter,* **22**, 312201, (2010).

[29] L. Yu and A. Zunger, "A polarity-induced defect mechanism for

conductivity and magnetism at polar–nonpolar oxide interfaces", *Nat. Commun.,* **5**, 6118, (2014).

[30] M. Huijben, G. Koster, M. K. Kruize, S. Wenderich, J. Verbeeck, S. Bals, E. Slooten, B. Shi, H. Molegraaf, J. E. Kleibeuker, S. van Aert, J. B. Goedkoop, A. Brinkman, D. H. A. Blank, M. S. Golden, G. van Tendeloo, H. Hilgenkamp and G. Rijnder, "Defect Engineering in Oxide Heterostructures by Enhanced Oxygen Surface Exchange", *Advanced Functional Materials,* **23**, 5240, (2013).

[31] N. Reyren, S. Gariglio, A. D. Caviglia, D. Jaccard, T. Schneider and J.-M. Triscone, "Anisotropy of the superconducting transport properties of the LAO/STO interface", *Appl. Phys. Lett.,* **94**, 112506, (2009).

[32] A. S. Kalabukhov, Y. A. Boikov, I. T. Serenkov, V. I. Sakharov, V. N. Popok, R. Gunnarsson, J. Borjesson, N. Ljustina, E. Olsson, D. Winkler and T. Claeson, "Cationic Disorder and Phase Segregation in $LaAlO_3/SrTiO_3$ Heterointerfaces Evidenced by Medium-Energy Ion Spectroscopy", *Phys. Rev. Lett.,* **103**, 146101, (2009).

[33] N. Mohanta and A. Taraphder, "Oxygen vacancy clustering and pseudogap behaviour at the $LaAlO_3/SrTiO_3$ interface", *J. Phys.: Condens. Matter,* **26**, 215703, (2014).

[34] J. Biscaras, N. Bergeal, S. Hurand, C. Feuillet-Palma, A. Rastogi, R. C. Budhani, M. Grilli, S. Caprara and J. Lesueur, "Multiple quantum criticality in a two-dimensional superconductor", *Nature Materials,* **12**, 542, (2013).

[35] J. Biscaras, N. Bergeal, S. Hurand, C. Grossetete, A. Rastogi, R. C. Budhani, D. LeBoeuf, C. Proust and J. Lesueur, "Two-Dimensional Superconducting Phase in $LaTiO_3/SrTiO_3$ Heterostructures Induced by High-Mobility Carrier Doping", *Phys. Rev. Lett.,* **108**, 247004, (2012).

[36] C. Bell, S. Harashima, Y. Kozuka, M. Kim, B. G. Kim, Y. Hikita and H. Y. Hwang, "Dominant Mobility Modulation by the Electric Field Effect at the $LaAlO_3/SrTiO_3$ Interface", *Phys. Rev. Lett.,* **103**, 226802, (2009).

[37] N. Scopigno, D. Bucheli, S. Caprara, J. Biscaras, N. Bergeal, J. Lesueur and M. Grilli, "Phase Separation from Electron Confinement at Oxide Interfaces", *Phys. Rev. Lett.,* **116**, 026804,

(2016).

[38] S. Caprara, J. Biscaras, N. Bergeal, D. Bucheli, S. Hurand, C. Feuillet-Palma, A. Rastogi, R. C. Budhani, J. Lesueur and M. Grilli, "Multiband superconductivity and nanoscale inhomogeneity at oxide interfaces", *Phys. Rev. B,* **88**, 020504, (2013).

[39] S. J. Pearton and D. P. Norton, "Dry etching of electronic oxides, polymers, and semiconductors", *Plasma Processes and Polymers,* **2**, 16, (2005).

[40] D. W. Reagor and V. Y. Butko, "Highly conductive nanolayers on strontium titanate produced by preferential ion-beam etching", *Nature Materials,* **4**, 593, (2005).

[41] D. Kan, T. Terashima, R. Kanda, A. Masuno, K. Tanaka, S. Chu, H. Kan, A. Ishizumi, Y. Kanemitsu and Y. Shimakawa, "Blue-ligh emission at room temperature from Ar^{+}-irradiated $SrTiO_3$", *Nature Materials,* **4**, 816, (2005).

[42] H. Gross, N. Bansal, Y. Kim and S. Oh, " In Situ Study of Emerging Metallicity on Ion-bombarded $SrTiO_3$ Surface", *J. Appl. Phys,* **110**, 073704, (2011).

[43] C. Schneider, S. Thiel, G. Hammerl, C. Richter and J. Mannhart, " Microlithography of Electron Gases Formed at Interfaces in Oxide Heterostructures", *Appl. Phys. Lett.,* **89**, 122101, (2006).

[44] N. Banerjee, M. Huijben, G. Koster and G. Rijnders, " Direct Patterning of Functional Interfaces in Oxide Heterostructures", *Appl. Phys. Lett.,* **100**, 041601, (2012).

[45] Y. Z. Chen, N. Bovet, F. Trier, D. V. Christensen, F. M. Qu, N. H. Andersen, T. Kasama, W. Zhang, R. Giraud, J. Dufouleur, T. S. Jespersen, J. R. Sun, A. Smith, J. Nygård, L. Lu, B. Büchner, B. G. Shen, S. Linderoth and N. Pryds, "A high-mobility two-dimensional electron gas at the spinel/perovskite interface of γ-$Al2O_3/SrTiO_3$", *Nat. Commun.,* **4**, 1371, (2012).

[46] Y. Z. Chen, N. Bovet, T. Kasama, W. W. Gao, S. Yazdi, C. Ma, N. Pryds and S. Linderoth, "Room Temperature Formation of High-Mobility Two-Dimensional Electron Gases at Crystalline Complex Oxide Interfaces", *Adv. Mater.,* **26**, 1462, (2014).

[47] C. Cen, S. Thiel, G. Hammerl, C. W. Schneider, K. E. Andersen, C. S. Hellberg, J. Mannhart and J. Levy, “Nanoscale Control of an Interfacial Metal–Insulator Transition at Room Temperature”, *Nature Materials,* **7**, 298, (2008).

[48] M. Kawasaki, K. Takahashi, T. Maeda, R. Tsuchiya, M. Shinohara, O. Ishiyama, T. Yonezawa, M. Yoshimoto and H. Koinuma, “Atomic Control of the SrTiO3 Crystal Surface”, *Science,* **266**, 1540, (1994).

[49] A. Ichimiya and C. P. I., Reflection High Energy Electron Diffraction, Cambridge: Cambridge University Press, (2004).

[50] H. Frederikse, W. Thurber and W. Hosler, “Electronic Transport in Strontium Titanate”, *Phys. Rev.* **134**, 444, (1964).

[51] J. Ziegler, J. Biersak and U. Littmark, The Stopping of Ions in Matter; www.srim.org., New York: Pergamon, (1985).

[52] P. P. Aurino, A. Kalabukhov, N. Tuzla, E. Olsson, T. Claeson and D. Winkler, “Nano-patterning of the electron gas at the $LaAlO_3/SrTiO_3$ interface using low-energy ion beam irradiation”, *Appl. Phys. Lett.,* **102**, 201610, (2013).

[53] J. J. Cuomo, S. M. Rossnagel and H. Kaufman, Handbook of Ion Beam Processing Technology - Principles, Deposition, Film Modification and Synthesis, Noyes: William Andrew Publishing, (1989).

[54] F. Bi, D. F. Bogorin, C. Cen, C. Bark, J. W. Park, C. B. Eom and J. Levy, “"Water-cycle" mechanism for writing and erasing nanostructures at the $LaAlO_3/SrTiO_3$ interface”, *Appl. Phys. Lett.,* **97**, 173110, (2010).

[55] Y. Xie, Y. Hikita, C. Bell and H. Y. Hwang, “Control of electronic conduction at an oxide heterointerface using surface polar adsorbates”, *Nat. Commun.,* **2**, 494, (2011).

[56] M. Huang, G. Jnawli, J.-F. Hsu, S. Dhingra, H. Lee, S. Ryu, F. Bi, F. Ghahari, J. Ravichandran, L. Chen, P. Kim, C.-B. Eom, B. D'Urso, P. Irvin and J. Levy, “Electric field effects in graphene/$LaAlO_3/SrTiO_3$ heterostructures and nanostructures”, *APL Mater.,* **3**, 062502, (2015).

[57] J. R. Vig, “UV/ozone cleaning of surfaces”, *J. Vac. Sci. Technol. A,* **3**, 1027, (1985).

[58] M. Lee, J. R. Williams, S. Zhang, C. D. Frisbie and D. Goldhaber-Gordon, “Electrolyte Gate-Controlled Kondo Effect in $SrTiO_3$”, *Phys. Rev. Lett.,***107**, 256601, (2011).

[59] R. Borgani, D. Forchheimer, J. Bergqvist, P.-A. Thorén, O. Inganas and D. Haviland, “Intermodulation electrostatic force microscopy for imaging surface photo-voltage”, *App. Phys. Lett.,* **105**, 143113, (2014).

[60] S. Caprara, D. Bucheli, N. Scopigno, N. Bergeal, J. Biscaras, S. Hurand, J. Lesueuer and M. Grilli, “Inhomogeneous multi carrier superconductivity at $LaXO_3/SrTiO_3$ (X = Al or Ti) oxide interfaces”, *Supercond. Sci. Technol.,* **28**, 014002, (2015).

[61] M. Huijben, G. Koster, M. K. Kruize, S. Wenderich, J. Verbeeck, S. Bals, E. Slooten, B. Shi, H. Molegraaf, J. E. Kleibeuker, S. van Aert, J. B. Goedkoop, A. Brinkman, D. H. A. Blank, M. S. Golden, G. van Tendeloo, H. Hilgenkamp and G. Rijnder, “Defect Engineering in Oxide Heterostructures by Enhanced Oxygen Surface Exchange”, *Advanced Functional Materials,* **42**, 5240, (2013).

[62] N. Reyren, S. Thiel, A. D. Caviglia, L. Fitting-Kourkoutis, G. Hammer, C. Richter, C. W. Schneider, T. Kopp, A.-S. Räuetschi, D. Jaccard and e. al., “Superconducting Interfaces between Insulating Oxides”, *Science,* **317**, 1196, (2007).

[63] C. S. Koonce, M. L. Cohen, J. F. Schooley, W. R. Hosler and E. R. Pfeiffer, “Superconducting transition temperatures of semiconducting $SrTiO_3$”, *Phys. Rev.,* **2**, 380, (1967).

[64] J. F. Schooley, H. P. R. Frederikse, W. R. Hosler and E. R. Pfeiffer, “Superconductive properties of ceramic mixed titanates”, *Phys. Rev.,* **2**, 301, (1967).

[65] R. M. Fernandes, Haraldsen J. T., P. Wolfle and A. V. Balatsky, “Two-band superconductivity in doped SrTiO3 films and interfaces”, *Phys. Rev. B,* **87**, 014510, (2013).

[66] C. Richter, H. Boschker, W. Dietsche, E. Fillis-Tsirakis, R. Jany, F. Loder, L. F. Kourkoutis, D. A. Muller, J. R. Kirtley, C. W.

Schneider and J. Mannhart, “Interface superconductor with gap behaviour like a high-temperature superconductor”, *Nature,* **502**, 528, (2013).

[67] D. Bucheli, S. Caprara and M. Grilli, “Pseudo-gap as a signature of inhomogeneous superconductivity in oxide interfaces”, *Supercond. Sci. Technol.,* **28**, 045004, (2015).

[68] R. Arpaia, S. Charpentier, R. Toskovic, T. Bauch and F. Lombardi, “$YBa_2Cu_3O_7$ nanorings to probe fluxoid quantization in high critical temperature superconductors”, *Physica C,* **506**, 184, (2014).

[69] K. K. Likharev, “Superconducting weak links”, *Rev. Mod. Phys.,* **51**, 101, (1979).

[70] W. J. Skocpol, M. R. Beasley and M. Tinkham, “Phase-Slip Centers and Nonequilibrium Processes in Superconducting Tin Microbridges”, *J. Low Temp. Phys.,* **65**, 145, (1974).

[71] K. K. Likharev, “Vortex motion and the Josephson effect in superconducting thin bridges”, *Zh. Eksp. Teor. Fiz.,* **61**, 1700, (1971).

[72] M. V. Pedyash, G. J. Gerritsma, D. H. A. Blank and H. Rogalla, “Coherent Vortex Motion in Superconducting Nanobridges Based on YBaCuO Thin Films”, *IEEE Trans. Appl. Supercond.,* **5**, 1387, (1995).

[73] T. Bauch, F. Lombardi, F. Tafuri, A. Barone, G. Rotoli, P. Delsing and T. Claeson, “Macroscopic quantum tunneling in d-wave $YBa_2Cu_3O_{7-\delta}$ Josephson Junctions” *Phys. Rev. Lett.,* **94**, 087003, (2005).

[74] V. M. Krasnov, T. Golod, T. Bauch and P. Delsing, “Anticorrelation between temperature and fluctuations of the switching current in moderately damped Josephson junctions”, *Phys. Rev. B,* (76), 224517, (2007).

[75] L. Longobardi, D. Massarotti, G. Rotoli, D. Stornaiuolo, G. Papari, A. Kawakami, G. P. Pepe, A. Barone and F. Tafuri, “Thermal hopping and retrapping of a Brownian particle in the tilted periodic potential of a NbN/MgO/NbN Josephson junction”, *Phys. Rev. B,* 84, 184504, (2011).

[76] R. L. Kautz and J. M. Martinis, “Noise-affected I-V curves in small hysteretic Josephson junctions”, *Phys. Rev. B,* **42**, 9903, (1990).

[77] N. Mros, V. M. Krasnov, A. Yurgens, D. Winkler, and T. Claeson, "Multiple-valued c-axis critical current and phase locking in $Bi_2Sr_2CaCu_2O_{8+\delta}$ single crystals," *Phys. Rev. B*, **57**, 8135, (1998).

[78] V. Lefevre-Seguin, E. Turlot, C. Urbina, D. Esteve and M. H. Devoret, “Thermal activation of a hysteretic dc suyerconducting quantum interference device from its different zero-voltage states”, *Phys. Rev. B,* **46**, 5507, (1992).

[79] D. A. Dikin, M. Mehta, C. W. Bark, C. B. Folkman, C. B. Eom and V. Chandrasekhar, “Coexistence of Superconductivity and Ferromagnetism in Two Dimensions”, *Phys. Rev. Lett.,* **107**, 056802, (2011).

[80] A. A. Bannykh, J. Pfeiffer, V. S. Stolyarov, I. E. Batov, V. V. Ryazanov and M. Weides, “Josephson tunnel junctions with a strong ferromagnetic interlayer”, *Phys. Rev. B.,* **79**, 054501, (2009).

[81] F. S. Bergeret, A. F. Volkov and K. B. Efetov, “Odd triplet superconductivity and related phenomena in superconductor-ferromagnet structures”, *Rev. Mod. Phys.,* **77**, 1321, (2005).

[82] M. Eschrig, J. Kopu, J. C. Cuevas and G. Schon, “Theory of Half-Metal-Superconductor Heterostructures”, *Phys. Rev. Lett.,* **90**, 137003, (2003).